

UNIVERSITÄT OSNABRÜCK

Fachbereich Physik · Barbarastraße 7 · D-49076 Osnabrück

Studies on rare-earth silicide nanowires on vicinal silicon surfaces

A
thesis
presented for the
Master of Science degree
by Sören R. LINDEMANN (936813)

27th March 2014

Thesis committee:

Joachim WOLLSCHLÄGER (Universität Osnabrück)
Hanno H. WEITERING (The University of Tennessee)

Author Sören R. Lindemann
Student number 936813
Date of birth 07th August 1989
Address Lüpkers Kamp 3
49811 Lingen (Ems)
Germany
Contact +49 591 53689
solindem@uos.de

1st Advisor Prof. Dr. Joachim Wollschläger
Institution Universität Osnabrück
Fachbereich Physik
Barbarastraße 7
49076 Osnabrück
Germany
Contact +49 541 969 2651
joachim.wollschlaeger@uos.de

2nd Advisor Prof. Dr. Hanno H. Weitering
Institution The University of Tennessee
Department of Physics and Astronomy
1408 Circle Drive
Knoxville, TN 37996
United States of America
Contact +1 865 974 7841
hanno@utk.com

I confirm, that I have written the present thesis independently and without illicit assistance. I did not make use of others than the indicated aids and publications. Any text or contents from other authors' sources have been marked.

Ich versichere, dass ich die eingereichte Arbeit selbstständig und ohne unerlaubte Hilfe verfasst habe. Anderer als der von mir angegebenen Hilfsmittel und Schriften habe ich mich nicht bedient. Alle wörtlich oder sinngemäß den Schriften anderer Autoren entnommenen Stellen habe ich kenntlich gemacht.

Osnabrück, 27th March 2014

Osnabrück, den 27. März 2014

*Working hard to get my fill,
everybody wants a thrill.
Payin' anything to roll the dice,
just one more time.
Some will win, some will lose,
some were born to sing the blues.
Oh, the movie never ends,
it goes on and on and on and on!*

Jonathan Cain, Steve Perry, Neal Schon, 1981.

Acknowledgement

Although this part of a thesis usually comes somewhere between bibliography and back cover, I'd like to start with all the people that supported me during the past years and made this work possible:

First of all, a lot of thanks go to Prof. Dr. Joachim Wollschläger for the great time I had in his group. Thank you very much for supervising my daily work, sometimes even around the globe! I'll never forget your open door policy and your will to conquer even my most stupid questions. Many thanks also go to Prof. Dr. Hanno H. Weitering for taking over the second reference of this thesis. I'm really grateful for the weeks I was allowed to be part of your group.

In the same breath, I thank Saban Hus for letting me be *the millstone around your neck!* Thank you so much for all the things you taught me in- and outside the lab. Whenever you are planning to come to Germany, just let me know!

Many thanks go to the German Research Foundation and the University society Osnabrück e.V.! Both granted financial support that made my work at the University of Tennessee possible.

Furthermore, I thank all former and present members of the group *Dünne Schichten und Grenzflächen*, especially my office colleagues Dr. Daniel Bruns, Nico Pathé, and Jari Rodewald. I also want to mention Dr. Henrik Wilkens for reading parts of this work.

I'd also like to thank my family and friends, especially my parents Klaudia and Richard, my brother Eike, and my girlfriend Judith. I would not be me without you!



Universitätsgesellschaft
Osnabrück e.V.



Abstract

One subject of this thesis was the preparation of silicon (Si) with the surface orientation (100). This surface tends to dimerization and the creation of a $(2 \times 1)/(1 \times 2)$ -reconstruction, in order to (partially) saturate dangling bonds at the surface. Furthermore, vicinal Si(100) surfaces with a misorientation of 4° towards the $\langle 110 \rangle$ -direction were investigated. Due to the miscut and with regard to suitable preparation parameters, a surface with only (1×2) -reconstructed terraces can be provoked. The average terrace width in the ideal case is 3.89 nm. Hence, vicinal Si(100) can be used as substrate for the ordered and uni-directional growth of rare-earth silicide nanowire arrays, e.g. with yttrium di-silicide (YSi_2). Here, the inter-wire distance is adjustable by variation of the sample surface misorientation. YSi_2 grows epitaxially on Si(100) along the $[1\bar{1}0]$ -direction, since the lattice parameters almost match perfectly. In this context, measurements using Scanning Tunneling Microscopy (STM) and Reflection High-Energy Electron Diffraction (RHEED) were performed. Additionally, the crystallinity of the nanowires and the structure of the wetting layer were investigated.

Kurzfassung

Im Rahmen dieser Arbeit wurde die Präparation von Silizium (Si) mit der Oberflächenorientierung (100) optimiert. Diese neigt zur Dimerisierung und Ausbildung einer $(2 \times 1)/(1 \times 2)$ -Rekonstruktion, um freie Bindungen an der Oberfläche abzusättigen. Außerdem werden vizinale Si(100)-Oberflächen mit einem Fehlwinkel von 4° gegen die $\langle 110 \rangle$ -Richtung untersucht. Aufgrund des Fehlwinkels und mithilfe der geeigneten Präparationsparameter wird eine eindomänige Oberfläche herbeigeführt, die nur (1×2) -rekonstruierte Terrassen aufweist. Die mittlere Terrassenbreite beträgt im Idealfall 3,89 nm. Damit ist vizinales Si(100) als Substrat für das geordnete und uni-direktionale Aufwachsen von Selten-Erd-Silizid-Nanodrähten, wie z.B. Yttrium-Disilizid (YSi_2), mit einem über den Fehlwinkel variierbaren Drahtabstand geeignet. YSi_2 wächst epitaktisch auf Si(100) entlang der $[1\bar{1}0]$ -Richtung auf, da die Gitterkonstanten nahezu keine Fehlanpassung aufweisen. Hierzu wurden Messungen mit Scanning Tunneling Microscopy (STM) und Reflection High-Energy Electron Diffraction (RHEED) durchgeführt. Des Weiteren wurde die Kristallinität der Nanodrähte und die Struktur der ersten, benetzenden Ebene untersucht.

Contents

Acknowledgement

Abstract

Kurzfassung

Acronyms	III
List of Figures	VI
1 Introduction	1
2 Basics	3
2.1 Electron diffraction at crystal surfaces	3
2.1.1 Wave character of electrons	3
2.1.2 N-slit experiment	4
2.1.3 Reciprocal space	5
2.1.4 Kinematic analysis of surface scattering	6
2.2 RHEED	9
2.2.1 Origin of RHEED streaks	9
2.2.2 Vicinal surfaces	11
2.2.3 Experimental setup	14
2.3 Simplified vacuum tunneling	16
2.3.1 One-dimensional tunneling effect	16
2.3.2 Theory according BARDEEN, TERSOFF, and HAMANN	17
2.4 STM	18
2.4.1 Working principle	18
2.4.2 Tip preparation	19
2.4.3 Experimental setup	21
3 Investigated materials	25
3.1 Si	25
3.2 Y and its silicides	28
4 Results and discussion	31
4.1 Substrate preparation	31
4.2 YSi ₂ on flat silicon (Si)(100)	38
4.3 YSi ₂ on vicinal Si(100)	43
4.3.1 DC heating step-parallel	43
4.3.2 DC heating step-up	45

Contents

5 Conclusion	49
Bibliography	58

Acronyms

Al	aluminium
B	boron
CCM	constant current mode
CHM	constant height mode
CTR	crystal truncation rods
CU	control unit
DC	direct current
DFT	density functional theory
DoS	density of states
DWF	DEBYE-WALLER-factor
DySi₂	dysprosium di-silicide
fcc	face centered cubic
FIM	Field-Ion Microscopy
GIXRD	Grazing Incidence X-Ray Diffraction
hcp	hexagonal closed-package
KOH	potassium hydroxide
LEED	Low-Energy Electron Diffraction
MBE	Molecular Beam Epitaxy
MOKE	Magneto-Optic KERR Effect
Nd	neodymium
P	phosphorus
PA	post-annealing
PBN	pyrolytic boron nitride
REE	rare earth elements
RESN	rare-earth silicide nanowires
RHEED	Reflection High-Energy Electron Diffraction
RT	room temperature
sc	simple cubic

SEM	Scanning Electron Microscopy
Si	silicon
SiC	silicon carbide
SPALEED	Spot Profile Analysis Low-Energy Electron Diffraction
SPM	Scanning Probe Microscopy
STM	Scanning Tunneling Microscopy
UHV	ultra-high vacuum
UOS	Universität Osnabrück
UTK	The University of Tennessee in Knoxville
W	tungsten
XPS	X-ray Photoelectron Spectroscopy
XRD	X-ray Diffraction
Y	yttrium
YSi₂	yttrium di-silicide

List of Figures

2.1	1D N-slit experiment for $N = 4$ and $N = 100$; from Ref. [13]	4
2.2	EWALD-sphere using RHEED geometry	6
2.3	Kinematic analysis of surface scattering during RHEED	7
2.4	Idealized reciprocal lattice for three different cases; from Ref. [37]	9
2.5	Origin of RHEED streaks; from Ref. [8].	9
2.6	RHEED pattern (15 keV, electron beam in $\langle\bar{1}10\rangle/\langle1\bar{1}0\rangle$ direction) of clean, nominally flat Si(100) surface	10
2.7	STM image of clean, vicinal Si(100) surface with 4° miscut towards $\langle110\rangle$	11
2.8	Idealized vicinal surface and its reciprocal lattice; taken from Ref. [8]	12
2.9	RHEED pattern (15 keV, electron beam perpendicular to step edges) of clean, vicinal Si(100) surface with 4° miscut towards $\langle110\rangle$	13
2.10	Schematic illustration of RHEED geometry	14
2.11	UHV chamber and RHEED setup at UTK	15
2.12	1D tunnel junction between surface and STM tip; taken from Ref. [48]	16
2.13	STM in operation over a stepped surface; taken from Ref. [52]	19
2.14	SEM images of freshly prepared W STM tip; taken from Ref. [54]	20
2.15	Device for preparation of metal tips at UTK	20
2.16	UHV chamber and STM setup at UOS	23
3.1	Non-primitive fcc unit cell of Si; taken from Ref. [73]	25
3.2	Si(100) with and without (2×1) -reconstruction; taken from Ref. [14]	26
3.3	Vicinal Si(100) surface with dimer orientations; taken from Ref. [77]	26
3.4	Si(100)-wafer with 4° miscut towards $\langle110\rangle$	27
3.5	Bulk unit cell of YSi ₂ in AlB ₂ -structure	28
3.6	Cross-sectional and side view of YSi ₂ surface unit cells; taken from Ref. [86]	29
4.1	STM image (CCM, $V_T = -1.5$ V, $J_{set} = 0.07$ nA) of vicinal Si(100) with DC heating step-down	32
4.2	STM image (CCM, $V_T = -1.5$ V, $J_{set} = 0.1$ nA) of vicinal Si(100) with DC heating step-down and PA	33
4.3	STM image (CCM, $V_T = -2.0$ V, $J_{set} = 0.1$ nA) of vicinal Si(100) with DC heating step-up	34
4.4	STM image (CCM, $V_T = -1.5$ V, $J_{set} = 0.1$ nA) of vicinal Si(100) with DC heating step-up and PA	35
4.5	Height profile along the line scan in Fig. 4.4	35
4.6	STM image (CCM, $V_T = -1.5$ V, $J_{set} = 0.1$ nA) of vicinal Si(100) with DC heating step-parallel	36

4.7	STM image (CCM, $V_T = -1.5$ V, $J_{\text{set}} = 0.05$ nA) of vicinal Si(100) with DC heating step-parallel and PA	37
4.8	STM image (CCM, $V_T = -1.5$ V, $J_{\text{set}} = 0.1$ nA) of YSi ₂ -nanowires on vicinal Si(100) with DC heating step-parallel after PA procedure	37
4.9	RHEED pattern (15 keV, electron beam in $\langle \bar{1}10 \rangle / \langle 1\bar{1}0 \rangle$ direction) of flat Si(100) surface with and without Y-coverage ($\theta \approx 0.35$ ML)	39
4.10	RHEED pattern (15 keV, electron beam in $\langle \bar{1}10 \rangle / \langle 1\bar{1}0 \rangle$ direction) of Si(100) surface in Fig. 4.9 a) without post-processing	40
4.11	Magnification of black frame in Fig. 4.9 b)	41
4.12	RHEED pattern of sample in Fig. 4.9 with azimuth $\gamma \approx 255^\circ$ as evidence for crystallinity and good lattice match of nanowires	42
4.13	RHEED pattern (15 keV, electron beam perpendicular to step edges, step-parallel DC) of vicinal Si(100) surface with and without Y-coverage ($\theta \approx 0.4$ ML)	44
4.14	RHEED pattern (15 keV, electron beam parallel to step edges, step-up DC) of vicinal Si(100) surface with and without Y-coverage ($\theta \approx 0.35$ ML)	47
4.15	RHEED pattern of sample in Fig. 4.14 with azimuth $\gamma \approx 255^\circ$ as evidence for crystallinity and good lattice match of nanowires	48

1 Introduction

The investigation of metallic and especially rare-earth silicide nanowires (RESN) sparked great interest within the past years. As silicon-based technology is shrinking to dimensions of less than 50 nm, new fabrication methods beyond conventional lithography become more and more important. One approach for reaching smaller sizes, e.g. in transistor technology, is self-assembly. For self-assembled electronic applications on the nanometer scale low-resistance electrodes or interconnects are necessary. Here, RESN get into game.

These form each other automatically on a heated silicon (Si) substrate and are strongly dependent on the growth parameters [1]. Many properties of atomic wires originate from their quasi one-dimensional shape. One aspect that has to be considered with decreasing dimensionality is the limitation of degrees of freedom. In this case, it can lead to plenty of interesting effects. RESN might help to understand the correlation of structural, electrical and magnetical properties in one-dimensional structures or might be suitable candidates to study complex physical problems like superconductivity or spin-charge-separation.

Self-assembled nanowires usually have atomically abrupt interfaces and can grow several microns long for widths and heights in the single digit nanometer range. In this thesis, the structural properties of yttrium di-silicide (YSi_2)-nanowires and coexisting nanophases will be studied on vicinal Si(100) surfaces with 4° misorientation towards the $\langle 110 \rangle$ -direction. Their uni-directional growth makes an anisotropic lattice mismatch necessary. Hence, the formation of RESN has already been studied intensively on flat Si(100) [2–7]. This research will be expanded by Scanning Tunneling Microscopy (STM) and Reflection High-Energy Electron Diffraction (RHEED) measurements from vicinal Si(100).

2 Basics

In this chapter the experimental methods used and their theoretical foundations will be introduced. Both, the Si substrates as well as the RESN have been characterized by RHEED and STM. These techniques may be found in Sec. 2.2 and Sec. 2.4. Basic information about electron diffraction, which is useful for understanding the processes during RHEED, will be introduced in Sec. 2.1. In the following, the term *current direction* is associated with the conventional direction of positive charges, which points in the opposite direction of the electron flow.

2.1 Electron diffraction at crystal surfaces

2.1.1 Wave character of electrons

Electrons may be treated as particles and waves, which is known as the wave-particle dualism. This leads to the fact that electron beams can experience optical phenomena, e.g. refraction, reflection, and diffraction [8]. Non-relativistic particles in general have a characteristic wavelength, the so called DE BROGLIE-wavelength

$$\lambda = \frac{h}{p} = \sqrt{\frac{h^2}{2m \cdot E_{\text{kin}}}} . \quad (2.1)$$

Here, h denotes the PLANCK-constant, p the momentum, m the mass, and E_{kin} the kinetic energy [9]. If the absolute value of the wave vector $\mathbf{k} = 2\pi / \lambda \cdot \mathbf{e}_k$ is inserted into Eq. (2.1) taking into account the vectorial character of the momentum, one obtains

$$\mathbf{p} = \hbar \mathbf{k} . \quad (2.2)$$

Relativistic particles, e.g. electrons with high kinetic energies ($E_{\text{kin}} \gtrsim 50 \text{ keV}$), also have an equivalent DE BROGLIE-wavelength. But then Eq. (2.1) and Eq. (2.2) have to be modified due to relativistic effects [8]. Anyway, the wave character of electrons makes interference possible and can lead to diffraction phenomena. Those may be observed when electrons hit a periodic assembly of scatterers, e.g. atoms in a single crystal. Further details concerning the wave character of electrons would go beyond the scope of this introduction and can be found in Ref. [8] and Ref. [10]. Anyway, an overview of the scattering at periodic assemblies will be given in Sec. 2.1.2. For the understanding of diffraction phenomena the reciprocal lattice is useful, which is described in Sec. 2.1.3 with a focus on RHEED. The kinematic approximation for electron diffraction at crystal surfaces is introduced in Sec. 2.1.4.

2.1.2 N-slit experiment

If electrons are incident on the periodic lattice of a crystalline solid, each atom behaves as a scattering center. Hence, the whole process can be understood as a typical N-slit experiment and each atom corresponds to a source of radial waves. Since the dimensions are much larger than the wavelength, these can be written as plane waves

$$\psi(\mathbf{r}, t) = \psi_0 e^{-i\mathbf{k}\cdot\mathbf{r}}. \quad (2.3)$$

In this equation, \mathbf{r} defines the source position, ψ_0 the amplitude, and \mathbf{k} the wave vector. The mathematical derivation and solution of an one-dimensional N-slit experiment may be found, e.g., in Ref. [11] and Ref. [12]. The resulting intensity for N slits is

$$I_N(x) = |\psi(x)|^2 \propto I_0 \cdot \left| \frac{\sin(N \frac{a}{2} k \frac{x}{\delta})}{\sin(\frac{a}{2} k \frac{x}{\delta})} \right|^2 = I_0 \cdot \left| \frac{\sin(N\pi \frac{a}{\lambda} \frac{x}{\delta})}{\sin(\pi \frac{a}{\lambda} \frac{x}{\delta})} \right|^2. \quad (2.4)$$

Here, the distance between two neighboring scatterers is given by a , while N indicates their number. Note that x/δ results from the small-angle approximation, where δ labels the distance between scatterers and observation plane and x the (lateral) position in the observation plane. Furthermore, $k = 2\pi/\lambda$ is the absolute value of the wave vector \mathbf{k} (cf. Eq. (2.2)). For an arbitrary initial intensity I_0 this type of function is plotted for $N = 4$ and $N = 100$ in Fig. 2.1.

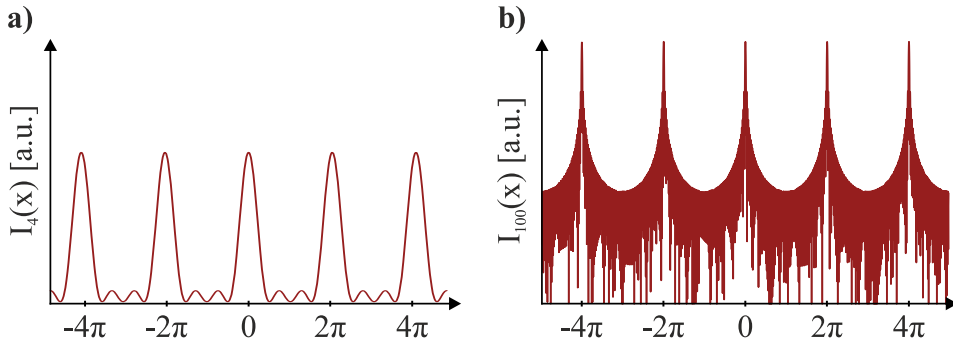


Figure 2.1: Solution of a one-dimensional N-slit experiment (cf. Eq. (2.4)) for **a)** $N = 4$ and **b)** $N = 100$. Main interference maxima are separated by integer multiples of 2π with $N - 2$ fringes in between and become sharper and more intense for an increasing number of slits. This image was taken and adapted from Ref. [13].

As can be seen from this image, the interference maxima become sharper and more intense for an increasing number of slits. But the simulated experiment shown in Fig. 2.1 just represents an idealized N-slit grating, while real diffraction patterns show decreasing intensity for higher diffraction orders. The reason for this are the shape and finite size of the slits so that an additional form factor has to be used as enveloping function in Eq. (2.4). This is generally applicable to any kind of scattering center, thus also to atoms of a crystal surface. The proper approximations will be further explained in Sec. 2.1.4 with a focus on electron diffraction at crystal surfaces.

2.1.3 Reciprocal space

Ideal single crystals are three-dimensional assemblies of atoms or groups of atoms, placed in a crystal lattice. Their surfaces can be understood as perfect interfaces between matter and vacuum. The reciprocal space is a mathematical concept useful for describing the diffraction at those surfaces [14–17], which will be briefly introduced in this chapter. The primitive translation vectors of the reciprocal lattice \mathbf{b}_j consistently have the dimension of a reciprocal length and satisfy the expression $\mathbf{a}_i \cdot \mathbf{b}_j = 2\pi \cdot \delta_{ij}$. Here, \mathbf{a}_i denotes the real space translation vectors, δ_{ij} is the KRONECKER-delta, and $i, j \in \mathbb{Z}$. For perfect surfaces the basis vectors in reciprocal space can be defined with a unit vector \mathbf{e}_n normal to the surface as

$$\begin{aligned}\mathbf{b}_1 &= 2\pi \cdot \frac{\mathbf{a}_2 \times \mathbf{e}_n}{\mathbf{a}_1 \cdot (\mathbf{a}_2 \times \mathbf{e}_n)} , \\ \mathbf{b}_2 &= 2\pi \cdot \frac{\mathbf{e}_n \times \mathbf{a}_1}{\mathbf{a}_1 \cdot (\mathbf{a}_2 \times \mathbf{e}_n)} .\end{aligned}\quad (2.5)$$

When electron waves with a wavelength of the same order of magnitude as typical lattice constants are incident at crystal surfaces, the resultant interference effects can be described by BRAGG's law [18]. From this it is known that constructive interference occurs, when the path difference of two scattered waves is equal to integer multiples of the wavelength. An alternative formulation are the LAUE-equations

$$\begin{aligned}\mathbf{a}_1 \cdot \mathbf{K}_{\parallel} &= 2\pi h , \\ \mathbf{a}_2 \cdot \mathbf{K}_{\parallel} &= 2\pi k .\end{aligned}\quad (2.6)$$

Here, $\mathbf{K} = \mathbf{k}_f - \mathbf{k}_i$ is the scattering vector and $\mathbf{K}_{\parallel} = \mathbf{k}_{f,\parallel} - \mathbf{k}_{i,\parallel}$ its component parallel to the surface [19]. As well, \mathbf{k}_i denotes the incident and \mathbf{k}_f the scattered wave vector, while $\mathbf{k}_{i,\parallel}$ and $\mathbf{k}_{f,\parallel}$ represent their projections into the surface plane, respectively. The items h and k are MILLER-indices [20], which correspond in their three-dimensional form to crystal lattice planes¹. Using Eq. (2.5) the parallel component of the scattering vector can also be expressed as linear combination of reciprocal lattice vectors

$$\mathbf{K}_{\parallel} = X \cdot \mathbf{b}_1 + Y \cdot \mathbf{b}_2 . \quad (2.7)$$

If the variables $X, Y \in \mathbb{R}$ attain integer values, they correspond to MILLER-indices. At these reciprocal lattice positions the LAUE-conditions in Eq. (2.6) are automatically fulfilled, i.e. the scattering vector is equal to a reciprocal lattice vector. Hence, constructive interference can be observed in equivalence to BRAGG's law. Since the LAUE-conditions are two-dimensional equations for diffraction at ideal surfaces, interference maxima occur as diffraction rods from the surface. This will be further explained in Sec. 2.1.4.

As one can see, the reciprocal space is a convenient concept, because reciprocal lattice vectors describe the periodicity of interference maxima like real space translation vec-

¹ MILLER-index k should not be confused with the absolute value of the wave vector $|\mathbf{k}|$ in Eq. (2.2).

tors describe the periodicity of unit cells [21]. Since the electrons are considered to be diffracted elastically, \mathbf{k}_i and \mathbf{k}_f have equal lengths. Thus, the solutions of Eq. (2.7) lie on a spherical surface with radius $2\pi/\lambda$. This construction is called EWALD-sphere and equivalent to a quasi-momentum conservation [22]. Its two-dimensional projection is sketched as a circle section in Fig. 2.2.

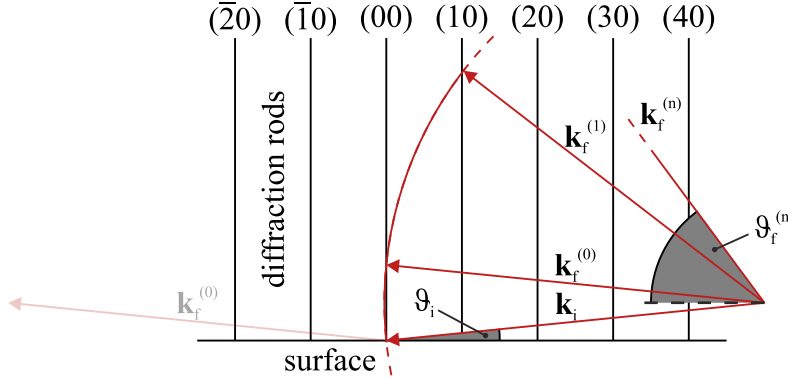


Figure 2.2: EWALD-sphere for electron diffraction at ideal surfaces using RHEED geometry. Here, \mathbf{k}_i is the incident wave vector and ϑ_i its angle at the surface. Scattered waves are represented by $\mathbf{k}_f^{(n)}$ and $\vartheta_f^{(n)}$, where (n) indicates the diffraction order. Constructive interference occurs where EWALD-sphere and diffraction rods intersect.

From this image it can be seen that constructive interference occurs, where the EWALD-sphere and the diffraction rods intersect. If non-ideal and especially stepped surfaces are investigated with electron diffraction, the perpendicular component of the scattering vector has to be taken in account as well [23]. Due to the path difference at atomic steps, additional interference effects appear. Therefore, both the reciprocal lattice vector in Eq. (2.7) as well as the scattering conditions in Eq. (2.6) have to be expanded into the third dimension. However, it should be noticed that the LAUE-equations only give information about the periodicity of the crystal lattice (!), whereas the inner structure of unit cells may have an influence on the diffraction intensity, too. From X-ray Diffraction (XRD) it is known that forbidden diffraction features can occur from destructive interference effects within the unit cells [21].

2.1.4 Kinematic analysis of surface scattering

Some applications in electron diffraction call for a precise analysis of the interference maxima, e.g. the RHEED intensity oscillation technique during Molecular Beam Epitaxy (MBE) [10, 24]. The interpretation of experimental data requires dynamic diffraction theory in such cases, which considers multiple scattering processes within the topmost atomic layers of the surface [25]. However, the intensity oscillation technique is not feasible for the systems investigated, since the growth mode is not subject of this work and in particular this method is not sensitive to sub-monolayer structures. Besides, the dynamic interpretation becomes rather complex for non-ideal surfaces. The application of a kinematic approach neglecting multiple scattering in the atomic

layers close to the surface is justified, which also leads to sufficient results in many cases [23, 26]. A schematic illustration of electron diffraction at a periodic assembly of atoms under grazing incidence is shown in Fig. 2.3.

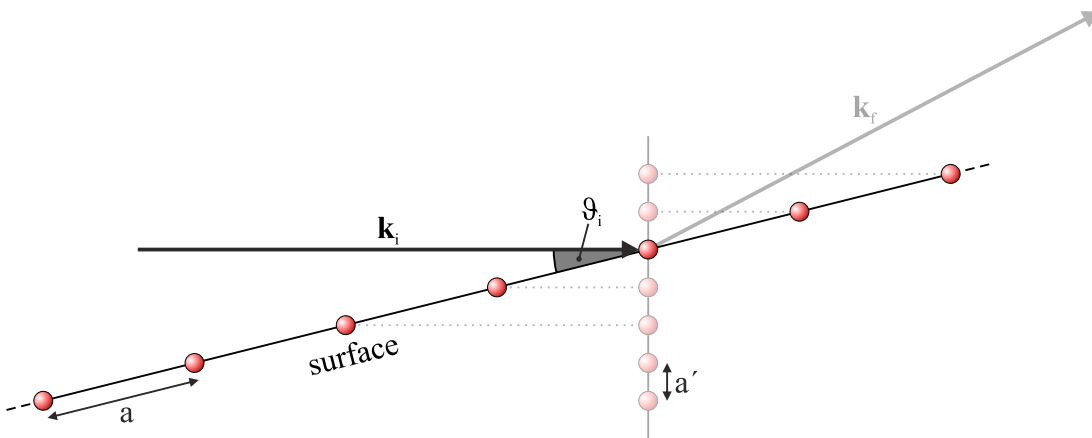


Figure 2.3: Kinematic analysis of scattering at ideal surfaces during RHEED. Since electrons are incident under the grazing angle ϑ , the atomic distance a can be translated to an effective lattice constant a' . The effective lattice is given by the projection of the ideal lattice into a plane perpendicular to the incident wave vector \mathbf{k}_i .

Scattering at ideal surfaces (with lattice constant a) under grazing incidence is equivalent to diffraction with orthogonal incidence by an effective lattice (with lattice constant a'). The projected atomic distances are much smaller than the ideal ones, because the sine in $a' = a \cdot \sin(\vartheta_i)$ becomes very small for grazing angles. Therefore, the energy of the electron beam has to be higher than for electron diffraction techniques with orthogonal incidence on the ideal surface in Fig. 2.3, e.g. Low-Energy Electron Diffraction (LEED). Otherwise, the fundamental BRAGG-condition for interference effects at crystal lattices would not be fulfilled, as λ would not have the same order of magnitude as the effective lattice constant. Although it was sketched one-dimensionally, the relation illustrated in Fig. 2.3 can be carried over to two dimensions without any loss of generality.

Anyhow, electron diffraction at crystal surfaces is an interaction between the particle waves and the periodic potential of the surface [27]. An extensive mathematical derivation of this interaction can be found in Ref. [28] and Ref. [29]. Since the experimental dimensions are much larger than λ (cf. Eq. (2.1)), it is feasible to apply the FRAUNHOFER-approximation and treat the electrons as plane waves. Hence, electron diffraction at a single electron can be expressed as

$$A_f(\mathbf{K}) = C A_i e^{i\mathbf{K} \cdot \mathbf{r}_e} \quad \text{with} \quad C = -\frac{\sin(\vartheta) q^2}{m c^2 \delta}. \quad (2.8)$$

$A_f(\mathbf{K})$ represents the amplitude of an elastically scattered electron wave, which follows directly from THOMSON-scattering at free particles. In this context A_i denotes the amplitude of the incident wave, \mathbf{K} the scattering vector (cf. Sec. 2.1.3), and \mathbf{r}_e the position of the single electron. Furthermore, ϑ is the scattering angle, q the electron

charge, m the electron mass, c the speed of light, and δ the distance between scattering center and observation point. Scattering at the electron cloud of a surface atom may be calculated by summation of the contribution of all its electrons using Eq. (2.8):

$$\begin{aligned} A_f(\mathbf{K}) &= C A_i \int d\mathbf{r} \varrho_{elec}(\mathbf{r}) e^{i\mathbf{K}\cdot(\mathbf{r}+\mathbf{r}_a)} = C A_i f(\mathbf{K}) e^{i\mathbf{K}\cdot\mathbf{r}_a} \\ \Rightarrow f(\mathbf{K}) &= \int d\mathbf{r} \varrho_{elec}(\mathbf{r}) e^{i\mathbf{K}\cdot\mathbf{r}} . \end{aligned} \quad (2.9)$$

Here, $f(\mathbf{K}) = \sum f_n(\mathbf{K})$ is the atomic form factor that considers the different positions \mathbf{r}_n of n electrons within the atom as phase differences. The item $\varrho_{elec}(\mathbf{r}) = \sum \varrho_n(\mathbf{r}_n)$ represents the time-averaged electron density distribution and results from the delocalization of the electrons, while \mathbf{r}_a is the atomic position and acts as reference point. Despite these considerations, the concept still does not completely describe the electronic surface interaction during RHEED. The potential distribution $\varphi(\mathbf{r})$ of a crystal surface results as well from the atomic nuclei as can be seen in

$$\nabla^2 \varphi(\mathbf{r}) = -4\pi [\varrho_{nucl}(\mathbf{r}) - \varrho_{elec}(\mathbf{r})] . \quad (2.10)$$

Regarding this, $\varrho_{nucl}(\mathbf{r})$ denotes the charge density contribution of the nuclei, while $\varrho_{elec}(\mathbf{r})$ is from Eq. (2.9). The FOURIER-transform of a scatterer's potential is defined as the amplitude of a scattered wave [28]. Inserting the inverse FOURIER-transform of the atomic potential distribution into Eq. (2.10) leads to the MOTT-formula

$$f_{MOTT}(\mathbf{K}) = 4\pi \frac{Z - f(\mathbf{K})}{K^2} . \quad (2.11)$$

In this context Z simply is the atomic number and $f(\mathbf{K})$ the scattering amplitude from Eq. (2.9). Therefore, the charge distributions of both the atomic nuclei as well as the electron clouds are considered. Due to the two-dimensional symmetry of a perfect and infinite surface without steps (cf. Fig 2.3), the diffraction pattern would consist of arbitrarily sharp diffraction rods [30]. But this result can not be achieved in real experiments, because the incident electrons always have a finite penetration depth at surfaces. Furthermore, the long-range order of crystal lattices, e.g., is disturbed by thermal vibrations, which is known as DEBYE-WALLER-factor (DWF) and reduces the peak-to-background ratio [31, 32]. Point defects in the crystal lattice have a similar effect on the diffuse background intensity, which is why they often are referred to as static DWF [33]. Besides, atomic steps broaden the diffraction rods at certain positions (between what would be BRAGG-points) [34, 35]. Regardless of the explicit electron diffraction technique, a complete understanding of the scattering at surfaces has to consider both the energy-dependent intensity and the shape of the diffraction features [36]. In fact, diffraction at real crystals leads to so called crystal truncation rods (CTR), which is a term out of the field of XRD. These are illustrated as a combination of BRAGG points and diffraction rods in Fig. 2.4 c) and represent a semi-infinite crystal [21]. A further explanation of RHEED patterns and the EWALD-sphere in relation to the RHEED specific geometry and vicinal surfaces is given in Sec. 2.2.2.

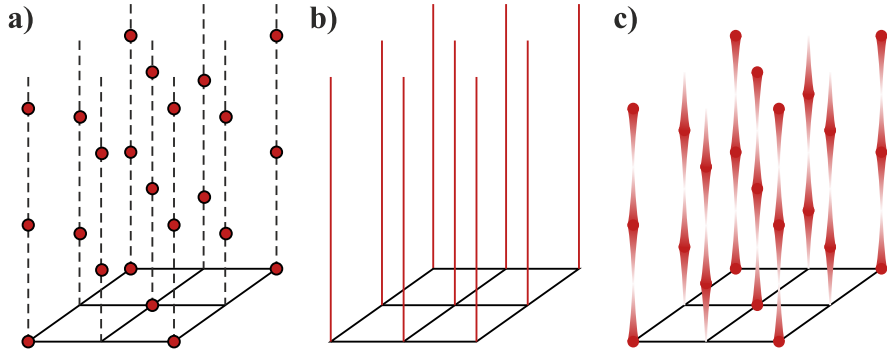


Figure 2.4: Idealized reciprocal lattices for **a)** three-dimensional crystals without defects (broken lines are just for better visibility), **b)** perfect and infinite surfaces, and **c)** semi-infinite surfaces. This image was taken and adapted from Ref. [37].

2.2 RHEED

2.2.1 Origin of RHEED streaks

RHEED is a powerful tool for the characterization of structural surface properties and was developed by NISHIKAWA and KIKUCHI [8, 38]. It is based on the elastic scattering of electrons at crystal lattices, which was discovered by DAVISSON, GERMER, and THOMSON [39–42]. The origin of RHEED streaks is explained in Fig. 2.5.

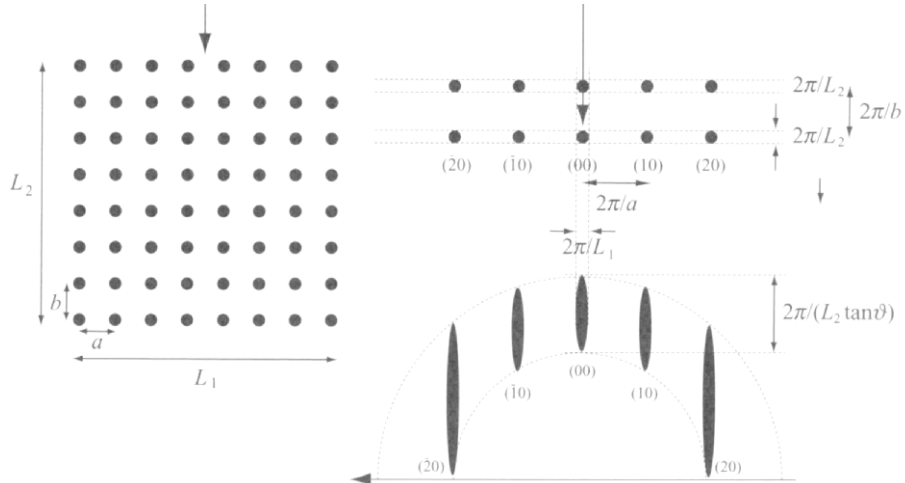


Figure 2.5: Schematic illustration of the origin of RHEED patterns. On the left a two-dimensional lattice is shown, where the finite sizes L_1 and L_2 are integer multiples of the lattice constants a and b , respectively. L_1 is perpendicular, L_2 parallel to the incident electron beam, which is indicated by the arrow above. The corresponding reciprocal lattice can be found on the upper, the simulated RHEED pattern on the lower right. The dimensions of the diffraction features depend on the items L_1 and L_2 and the incidence angle ϑ . This image was taken and adapted from Ref. [8].

From this image it can be seen that the average terrace size, which is represented by the finite sizes L_1 and L_2 , as well as the incidence angle ϑ influence the dimensions of

occurring diffraction features. In the simulated RHEED pattern in the lower right of Fig. 2.5 the vertical length of the streaks is proportional to $(L_2)^{-1}$. Thus, elongated streaks can be observed, if the terrace dimension is short parallel to the incident electron beam (small L_2). In contrast, spot-like streaks appear for terraces whose mean dimension is large parallel to the electron beam. The lattice constants a and b have effect on the position of the streaks and the distance between the LAUE-circles, since they are related to the reciprocal lattice vectors via Eq. (2.5).

The diffraction pattern of a clean, nominally flat Si(100) surface is shown in Fig. 2.6.

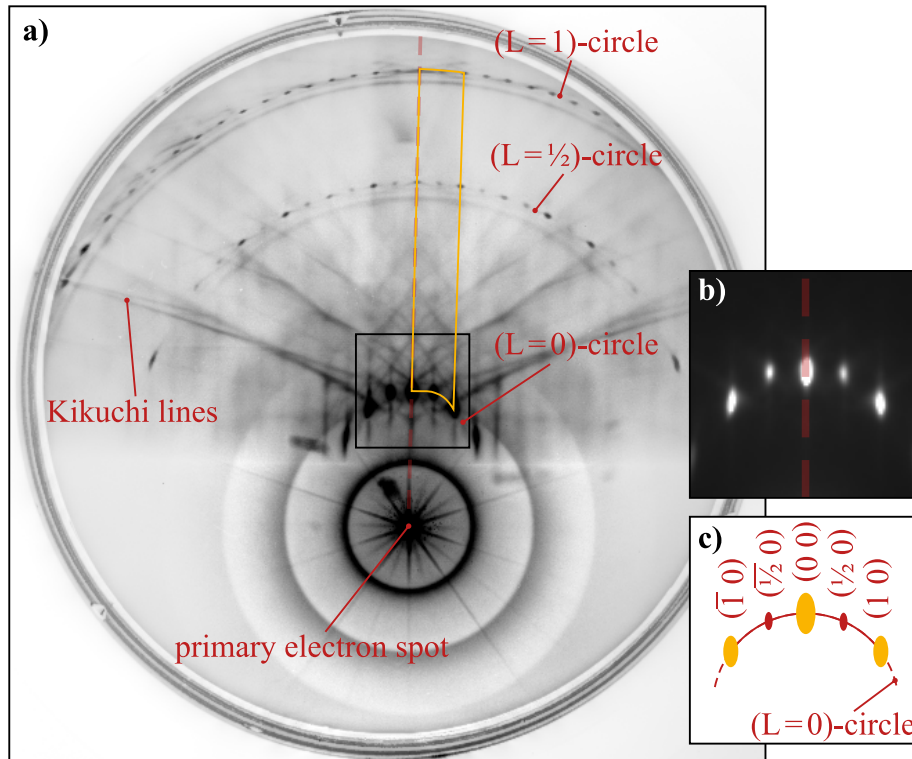


Figure 2.6: RHEED pattern (15 keV, electron beam in $\langle\bar{1}10\rangle/\langle1\bar{1}0\rangle$ direction) of a flat Si(100) surface. **a)** Inverted diffraction pattern with enhanced dynamic range. The yellow shape is attributed to the cubic (1×1) -lattice, the $(1/2 \ 0)$ - and $(\bar{1}/2 \ 0)$ -streaks as well as the $(L = 1/2)$ -circle to the $(2 \times 1)/(1 \times 2)$ -reconstruction of the Si(100) surface. **b)** Non-processed magnification of black rectangle in a). The (1×1) -streaks show higher intensities than those of the superstructure in between. **c)** Schematic drawing of $(L = 0)$ -circle in b).

The pattern in Fig. 2.6 a) exhibits a lot of characteristics, e.g. diffraction features of different shapes and intensities on three so called LAUE-circles. For an ideal surface (cf. Fig. 2.3) these would represent intersections of the diffraction rods with the EWALD-sphere, which are zones where the scattering condition (cf. Eq. (2.7)) is fulfilled. Since the diameter of the LAUE-circles is proportional to the inverse square of E_{kin} , more features occur on the phosphorescent screen at higher energies. Anyway, the bulk contribution of the single crystal can be seen as KIKUCHI-lines, which run from the primary electron spot to the edge of the image [38]. The four rings around the central

spot are no diffraction effects, but diffuse electrons that are inelastically scattered at the aperture and flange of the electron gun. Another artifact from the experimental setup is the shadow of the specimen, which appears brighter (because of the inverted contrast) in the lower third of this image. Surface and bulk inhomogeneities contribute to the greyish area left and right of the red dashed line.

On the one hand, the yellow shape in Fig. 2.6 a) has the (00)-, (01)-, (11)-, and (10)-streaks as corner points and can therefore be attributed to the cubic (1×1)-lattice of the surface. On the other hand, dimerization is a well-known phenomenon for Si(100), which will be explained in Sec. 3.1 and induces a $(2 \times 1)/(1 \times 2)$ -reconstruction. This leads to the $(\frac{1}{2} 0)$ - and $(\overline{\frac{1}{2}} 0)$ -streaks in the one and to the $(L = \frac{1}{2})$ -circle in the other reciprocal lattice direction². The additional streaks at the $(\frac{1}{2} \frac{1}{2})$ -position and integer multiples hereof are an artifact of the post-processing software and will be discussed in Sec. 4.2. Although the enhanced dynamic range increases the visibility of weak features, the resulting patterns can not be used for quantitative conclusions. Anyhow, the RHEED streaks have mostly dot-like shapes, which is why the average terrace width on this surface is supposed to be at least tens of nanometers. It was confirmed to be 49.2 nm over a large sample area using STM.

In general, RHEED patterns can also be used for quantitative measurements, e.g. to observe intensity oscillations of the specular beam. This technique allows to draw conclusions about different growth modes during MBE [24, 43, 44]. The interpretation of spot intensity variations, however, can be challenging when few is known about the coupling between substrate and adsorbate [45]. Besides, the RESN investigated in this work do not cover one full monolayer so that no oscillations would be visible at all. The diffraction method therefore was just used to qualitatively characterize the orientation of the dimer rows and nanowires on the Si surfaces.

2.2.2 Vicinal surfaces

Up to this point two-dimensional or at least atomically flat surfaces have been considered. In the following, diffraction at vicinal surfaces is introduced. These are cut and polished with an angle against one of the fundamental crystal axes, e.g. vicinal Si(100) with 4° towards $\langle 110 \rangle$ (cf. Fig. 2.7).

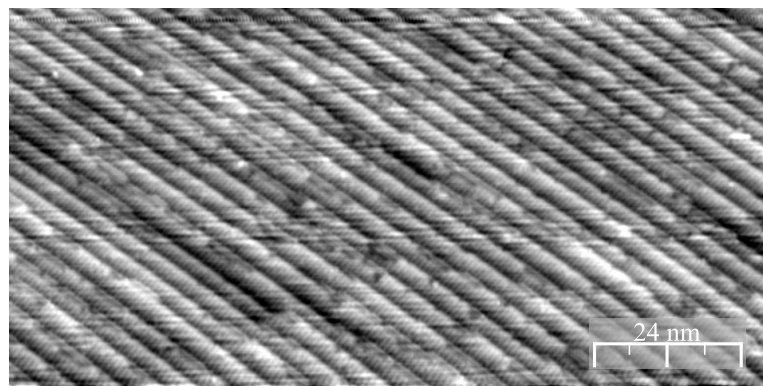


Figure 2.7: STM image of a clean, vicinal Si(100) surface with 4° miscut towards $\langle 110 \rangle$.

² Integer multiples of $(\frac{1}{2} 0)$ -streaks and $(L = \frac{1}{2})$ -circle result from this superstructure, too.

Typical features of a vicinal Si(100) surface can be observed: The step edges are parallel to each other and terraces show an homogenously distributed width. Furthermore, neighboring terraces are mostly separated by double steps, although a few single atomic steps can be found. Small kinks appear at a few sites, however, the terrace edges do not meander like it can be observed for flat surfaces. These properties make stepped surfaces suitable candidates for several scientific problems, e.g. the ordered growth of nanowire arrays [46]. An idealized vicinal surface without defects or inhomogeneities and the corresponding reciprocal lattice is shown in Fig. 2.8.

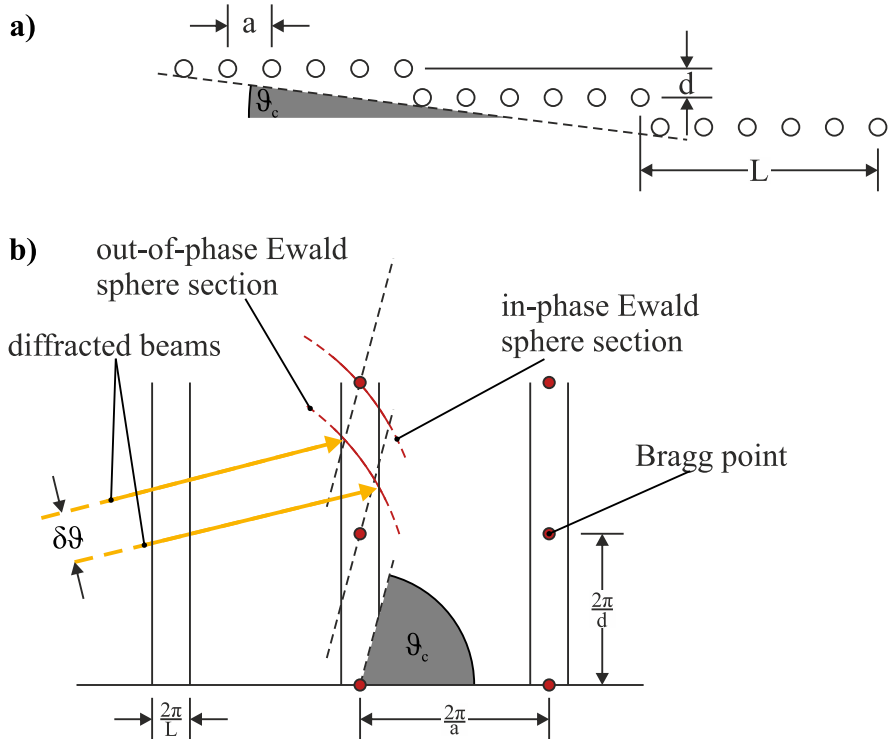


Figure 2.8: Idealized vicinal surface. **a)** Real space image with terraces that are equal in length L and step height d . Here, a determines the distance of nearest neighbors and ϑ_c the mean angle of misorientation. **b)** Corresponding reciprocal lattice with vertical diffraction rods (solid lines) and those tilted by ϑ_c (broken lines). In- and out-of-phase Ewald-spheres are indicated by red circle sections, three-dimensional BRAGG points by red dots. These images were taken and adapted from Ref. [8].

The EWALD-spheres are sketched as circle sections in this image. Where these pass through what would be BRAGG-points from an ideally three-dimensional single crystal, they are called in-phase EWALD-spheres, because the condition for constructive interference is fulfilled on their perimeter. On the contrary, out-of-phase Ewald-spheres appear when they pass through the middle of two BRAGG-points. The geometrical construction in Fig. 2.8 also illustrates that the diffraction conditions from stepped surfaces strongly depend on the mean angle of vicinality

$$\vartheta_c = \arctan \left(\frac{d}{L} \right). \quad (2.12)$$

Here, the step height is given by d and the average terrace width by L [8, 47]. Following this and the kinematic assumptions (cf. Sec. 2.1.4), the intensity of electrons that are scattered at an ideally vicinal surface can be calculated to

$$I(\mathbf{K}) \propto \left| \frac{\sin(N K_x \frac{a}{2})}{\sin(K_x \frac{a}{2})} \right|^2 \cdot \left| \frac{\sin(\frac{M}{2} (K_x L - K_z d))}{\sin(\frac{1}{2} (K_x L - K_z d))} \right|^2 . \quad (2.13)$$

Regarding this, \mathbf{K} denotes the scattering vector, K_x its x-, and K_z its z-component. N represents the mean number of scattering centers per terrace and M the number of steps. Hence, the first item corresponds to the average scattered intensity from one step with N terrace atoms. This is equivalent to the idealized one-dimensional N -slit experiment in Eq. (2.4). As can be derived from Fig. 2.8, the resulting diffraction rods from one perfect terrace alone (solid lines) would have the distance $2\pi/a$ and the width $2\pi/(N a) = 2\pi/L$. The second factor in Eq. (2.13) represents the number and order of the M terraces and leads to diffraction rods, which are normal to the miscut surface (broken lines). Their width parallel to the surface is $2\pi/\tau$, where $\tau = M \cdot \sqrt{d^2 + L^2}$ represents the length of the whole staircase.

The RHEED pattern of the vicinal Si(100) surface in Fig. 2.7 is shown in Fig. 2.9.

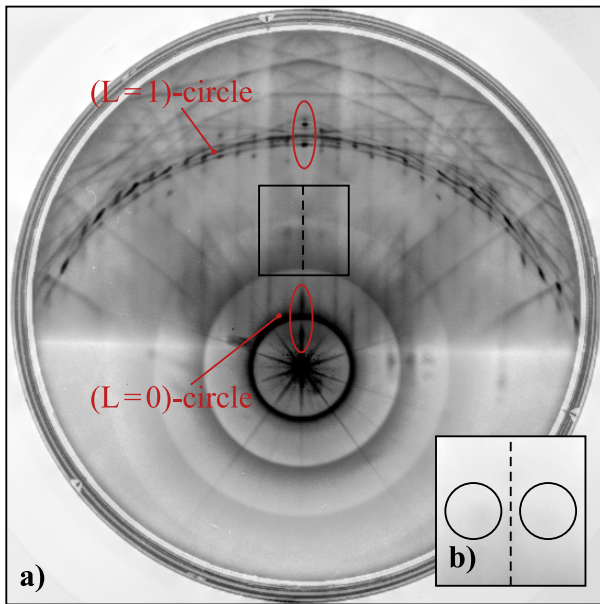


Figure 2.9: RHEED pattern (15 keV, electron beam perpendicular to step edges) of vicinal Si(100) **a)** with enhanced dynamic range and **b)** non-processed. The split spot in the black box is interpreted as first order of the ($L = 1/2$)-circle. As no higher orders can be observed, this indicates a minor (2×1)-domain at the surface. Spots that are split in the orthogonal direction are indicated by red ellipses and associated with the existence of mainly (1×2)-terraces.

A weak splitting can be observed left and right of where would be the ($0 \frac{1}{2}$)-streak in the black frame in Fig. 2.6 a). Since this is a manipulated RHEED pattern with enhanced dynamic range, the intensity of the various diffraction features can not be compared. Therefore, a non-processed magnification can be found in Fig. 2.6 b) with marks where the split spot is placed in Fig. 2.6 a). What is interpreted as first order of the ($L = 1/2$)-circle is even weaker in this image. As no higher orders can be observed at all, this probably indicates a minor (2×1) terrace orientation at the surface. Spots that are split along the (00)- or (01)-streak show a lot higher intensities (already before the image manipulation; not shown) and are indicated by red ellipses. They can be associated with the existence of mainly (1×2)-terraces of a small width, because the

pattern exhibits elongated streaks. This is not surprising, since the expected terrace width of the investigated Si(100) surfaces is $L_{\text{calc}} = d / \tan(\vartheta_c) \approx 3.89 \text{ nm}$.

2.2.3 Experimental setup

RHEED patterns are similar to those from LEED in at least three points: They result from electrons that are scattered at the periodic potential of the surface. Not less than high-vacuum is necessary to prevent the electron beam from interacting with residual gas molecules and the sample from absorbing impurities [14]. And both diffraction patterns can give information about structure and morphology of crystal surfaces. Since λ (cf. Eq. (2.1)) has the same order of magnitude as typical lattice constants, the fundamental condition for interference effects at crystal lattices is fulfilled. Although electrons with typically $8 \text{ keV} \leq E_{\text{kin}} \leq 20 \text{ keV}$ are used during RHEED (for some applications even higher), its surface sensitivity is ensured by grazing incidence of the electron beam at the sample surface. This geometry limits the information depth to the topmost atomic layers and keeps it comparable to the mean free path of low-energy electrons in matter, $\Lambda_{\text{LEED}} \lesssim 1 \text{ nm}$, even though the mean free path of high-energy electrons at orthogonal incidence is a lot higher. A schematic illustration of this geometry with dimensions of the present RHEED setup is shown in Fig. 2.10.

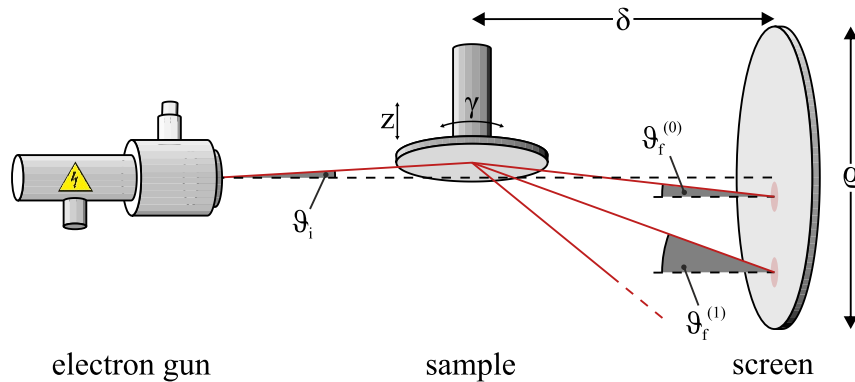


Figure 2.10: Schematic RHEED geometry with electron source (left), sample manipulator (center), and phosphorescent screen (right). In the present setup the distance between sample and screen is $\delta = 8.5 \text{ in} \approx 21.59 \text{ cm}$ and the screen diameter $\rho = 3.5 \text{ in} \approx 8.90 \text{ cm}$. Samples point downwards and can be varied in height z and azimuth angle γ . ϑ_i denotes the angle of incident and $\vartheta_f^{(n)}$ the angle of scattered electrons with (n) as diffraction order. Possible electron trajectories are indicated in red.

The basic setup consists of electron gun, sample holder, and phosphorescent screen. In the ultra-high vacuum (UHV) chamber, which was used at The University of Tennessee in Knoxville (UTK), the sample surfaces point downwards and can be manipulated in height z and azimuth angle γ . The distance between their rotation center and the window flange is $\delta = 8.5 \text{ in} \approx 21.59 \text{ cm}$ and the inner diameter of the screen is $\rho = 3.5 \text{ in} \approx 8.90 \text{ cm}$. The items ϑ_i and $\vartheta_f^{(n)}$ were already introduced in Sec. 2.1.3, they represent the angles of incident and diffracted electron beams. Possible trajectories

that occur during electron diffraction are represented by red lines in Fig. 2.10. A schematic illustration of the whole UHV chamber and two photographs of the RHEED setup can be seen in Fig. 2.11.

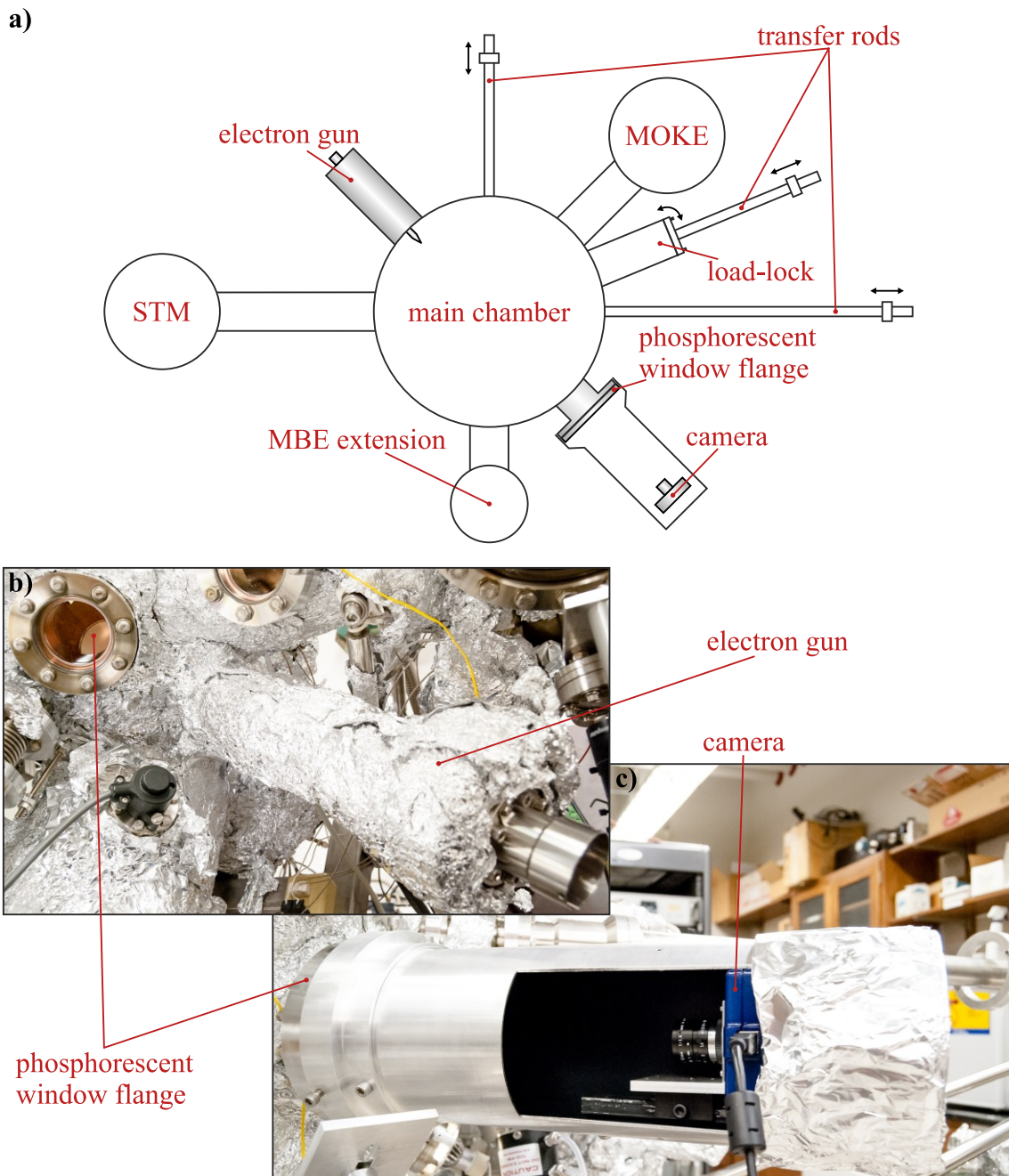


Figure 2.11: UHV chamber and RHEED setup at UTK. **a)** Schematic top view of UHV chamber with RHEED setup, STM extension, and in-situ MOKE. The manipulator is not shown, but would be orthogonal to this illustration in the center of the main chamber. **b)** Photograph of electron gun in the foreground and phosphorescent RHEED screen in the background. **c)** Photograph of camera extension.

2.3 Simplified vacuum tunneling

2.3.1 One-dimensional tunneling effect

From a quantum mechanical point of view electrons are delocalized and represented by the wave function $\psi(z)$, which is a solution of the one-dimensional and time-independent SCHRÖDINGER-equation

$$-\frac{\hbar^2}{2m} \frac{d^2}{dz^2} \psi(z) + U(z) \psi(z) = E \psi(z) . \quad (2.14)$$

Here, m denotes the electron mass, $U(z)$ the potential, and E the energy [48]. This leads to the phenomenon that particles can tunnel through barriers $U(z) > E$, which they classically could not surmount. In these classically forbidden regions, e.g. in a piecewise-constant potential barrier, Eq. (2.14) has the solution

$$\psi(z) = \psi(0) e^{-\kappa z} \quad \text{with} \quad \kappa = \frac{\sqrt{2m \cdot (U(z) - E)}}{\hbar} . \quad (2.15)$$

Regarding this, κ is the decay constant describing electron movement through the barrier and $\psi(0)$ represents the wave function at the sample-sided barrier edge. While the probability density $|\psi(z)|^2$ vanishes in classical mechanics, it attains non-zero values in quantum mechanics and leads to the tunneling effect [49]. The potential barrier is realized by a short vacuum gap between tip and surface in the case of STM. A schematic illustration can be found in Fig. 2.12.

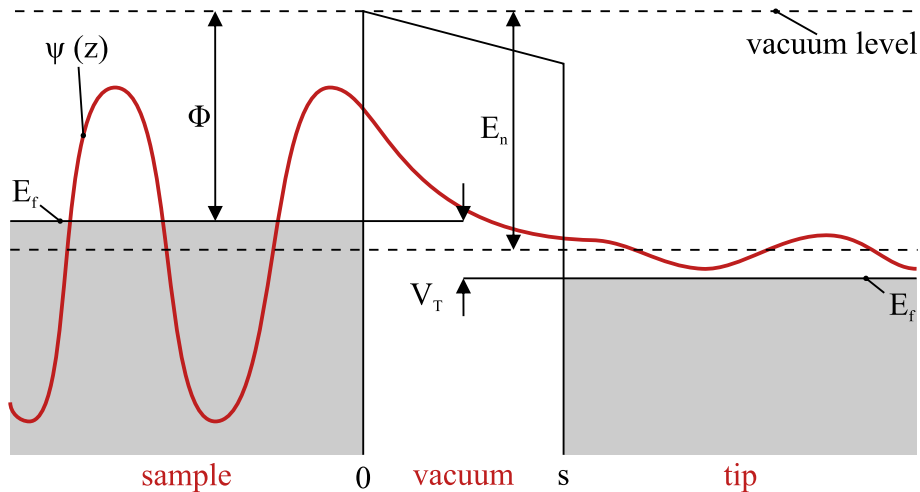


Figure 2.12: One-dimensional metal-vacuum-metal tunneling junction. The vacuum level $\Phi + E_f$ is the absolute value of the potential barrier, where Φ denotes the work funktion and E_f the FERMI-level. For small distances s and an applied bias voltage V_T the tunneling probability for a sample state $\psi(z)$ with the energy E_n increases ($E_f - V_T < E_n < E_f$). Despite the classically forbidden vacuum gap, a tunneling current J_T can be measured. This image was taken and adapted from Ref. [48].

A quantum-mechanical tunnel current $J_T \propto e^{-s/\kappa}$ is measured, when the potential barrier width s and the difference $(U(z) - E)$ in Eq. (2.15) are small. BINNIG and ROHRER found that the tunneling probability is additionally affected by an applied bias voltage V_T resulting in

$$J_T \propto \frac{V_T}{s} e^{-A\sqrt{\Phi}s}. \quad (2.16)$$

Here, $A = \frac{4\pi}{h} \sqrt{2m} \approx 1.025 (\sqrt{eV} \text{ \AA})^{-1}$ is the vacuum gap and Φ the average work function of the two electrodes, which is the minimum energy necessary to lift an electron into the vacuum level $\Phi + E_f$ (cf. Fig. 2.12). Hence, the tunneling probability of a surface state $\psi(z)$ with the energy E_n increases proportional to the bias voltage between tip and sample (for $E_f - qV_T < E_n < E_f$), since V_T lowers the effective barrier height [50–52]. Again, J_T is found to be very sensitive to s and only observable within a few Ångstrøm of barrier width [49].

This one-dimensional tunneling model leads to correct qualitative results. However, the exact influences of STM tip, tunneling barrier, and sample surface have to be expanded for quantitative issues [53, 54]. This is incorporated by the modified BARDEEN approach, which will be introduced in Sec. 2.3.2. A table of exemplary values for κ and Φ , however, is shown in Ref. [48]. An extensive derivation of the mathematical concept may be found in Ref. [55] and Ref. [56]

2.3.2 Theory according BARDEEN, TERSOFF, and HAMANN

A theoretical approach towards the tunneling of single electrons between two metals separated by an oxide layer was performed by BARDEEN long before the invention of STM [57]. In this work a transition matrix $M_{\mu\nu}$ was introduced, which treats the two electrodes as individual sub-systems. Therefore, two wave functions have to be regarded as solutions of the time-dependent SCHRÖDINGER-equation. This tunneling theory was complemented by the work of TERSOFF and HAMANN [58], who basically made three assumptions:

- 1)** The density of states (DoS) of the tip, ρ_{tip} , is considered to be constant.
- 2)** Only the foremost tip atom participates in the tunneling effect.
- 3)** Its wave function is considered to be a spherically symmetric s-orbital.

The first aspect takes into account that stable tips are required for the imaging during STM, whereas the second and third one express requirements concerning the tip shape. Since the two electrodes are not treated as one system as in Sec. 2.3.1, their wave functions ψ^{surf} and ψ^{tip} are assumed to not manipulate each other. According to the first-order, time-dependent perturbation theory, the tunneling process may then be understood in terms of a HAMILTON-transfer matrix [55]. This treatment implies that the tunneling distance always is a non-zero number and the bias voltage is small compared to the average work function. Thus, ψ^{surf} is not influenced by the resulting

electric field. The transition matrix $M_{\mu\nu}$ mentioned earlier can be calculated by the expression

$$M_{\mu\nu} = -\frac{\hbar^2}{2m} \int_{\text{edge}} dS [(\psi_\mu^{\text{tip}})^* \nabla \psi_\nu^{\text{surf}} - \psi_\nu^{\text{surf}} \nabla (\psi_\mu^{\text{tip}})^*] \quad (2.17)$$

The integral in this equation respects the size of the edge face separating sample surface and tip, which is nothing more than height and width of the potential barrier. Hence, according Ref. [57] one obtains for the tunneling current

$$J_T = \frac{4\pi q}{\hbar} \int_0^{V_T} d\epsilon \rho^{\text{surf}}(E_f - q \cdot V_T + \epsilon) \rho^{\text{tip}}(E_f + \epsilon) |M_{\mu\nu}|^2 . \quad (2.18)$$

Regarding this, q indicates the electron charge, ρ^{surf} the DoS of the surface, and ρ^{tip} the DoS of the tip. The item ϵ denotes the integration variable in terms of an energy. With respect to the three assumptions above, this relation can be simplified to

$$J_T \propto V_T \rho^{\text{surf}}(\mathbf{R}, E_f) . \quad (2.19)$$

Here, \mathbf{R} defines the position at the sample surface, which has the closest distance to the foremost tip atom. With this information at hand one can conclude that the topography one obtains from STM always images the DoS at the FERMI-level in dependence of the surface position and local environment. In reality, however, the apex does have an influence on the microscope resolution and ψ^{surf} and ψ^{tip} do affect each other at very short distances. Hence, the application of the TERSOFF-HAMANN-approximation is limited, which is subject of, e.g., Ref. [59] and Ref. [60].

2.4 STM

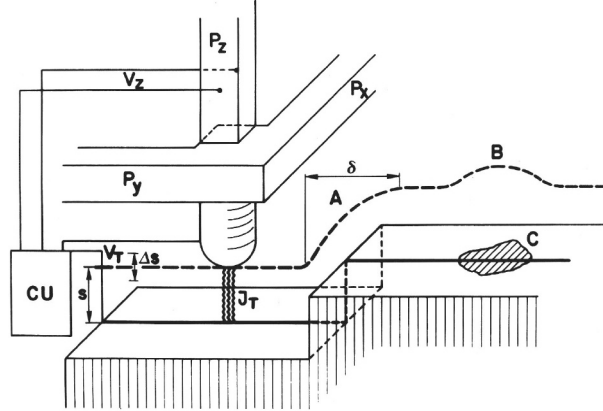
2.4.1 Working principle

STM was developed by BINNIG and ROHRER, earning them the Nobel Prize in Physics in 1986 [61, 62]. In cooperation with GERBER and WEIBEL they realized vacuum tunneling of electrons between sharp tungsten (W) tips and metal samples [63]. If this is combined with a high-precision scanner, microscopes with up to 0.1 nm lateral and 0.01 nm depth resolution can be constructed. Hence, the technique enables the investigation of solid surfaces with atomic precision (or even higher [64, 65]).

As shown in Eq. (2.16), J_T decreases exponentially with s . But for the interpretation of surface images by STM it is also important to know, whether electrons are tunneling into unoccupied or out of occupied surface states. The latter is usually associated with a positive gap voltage between tip and sample. Depending on the voltage level of V_T also electronic states of the valence or the conduction band can have an impact on the imaging results. Especially the material and shape of the tip as well as the chemical composition of the sample can affect the tunnel probability, which was indicated at the end of Sec. 2.3.2 already. Therefore, chemical information might be needed for a

correct interpretation of the topographical image of the surface. A schematic of STM in operation can be seen in Fig. 2.13.

Figure 2.13: STM in operation over a stepped surface. Piezo-electric elements P_x and P_y allow to move the tip parallel to the surface, while P_z controls the gap width by height variation of the tip. The CU detects the tunnel current J_T for an applied gap voltage V_T . Height variation of P_z and detection of J_T are combined in CCM, where surface topographies are reconstructed by a feedback loop. This image was taken and adapted from Ref. [52].



This image shows that two piezo-electric elements P_x and P_y allow the lateral movement of the probe scanner, while P_z controls the gap width between probe and sample by height variation of the tip. Since J_T is strongly depending on s , two different operation modes can be used in STM. During constant height mode (CHM), s is fixed and the varying tunnel current is detected as a function of surface position. This is applicable at even surfaces, because the risk of tip collisions with atomic steps or islands is very low. On the contrary, the constant current mode (CCM) should be used to gain structural information of surfaces with higher atomic roughness. A feedback loop with the control unit (CU) then compares J_T with a pre-defined set point at every position of the surface. If necessary, CU varies P_z and therefore the value of s , which avoids the mentioned tip collisions with coarse surface structures. It should be noted that the setup of three separate piezo-electric transducers is replaced by a single piezo-electric tube in most of nowadays STM designs, which improves the microscopic performance and tip stability. Besides, a tube scanner is easier to fabricate and incorporate into a STM setup [66]. The working principle stays the same, though.

2.4.2 Tip preparation

Empirical results and theoretical calculations (cf. Sec. 2.3.2) have shown that the tip geometry considerably influences the resolution of images given by STM [67, 68, and references therein]. Collisions with surface atoms, adsorption of residual gas molecules, and desorption of atoms by voltage pulses are just some examples of how the electronic or atomic structure at the very end of real tips can change. But all these processes are affecting the resolution of the microscope. A bent or flattened tip can lead to increasing noise or blurred images, also referred to as multiple-tip effect. Hence, it should be the experimentalist's goal to prepare the apex shape as sharp as possible. The tips used during this thesis were made from polycrystalline W wire with 0.25 mm diameter that was etched in 5 molar potassium hydroxide (KOH) solution. An exemplary Scanning Electron Microscopy (SEM) image of a freshly prepared STM tip is shown in Fig. 2.14.

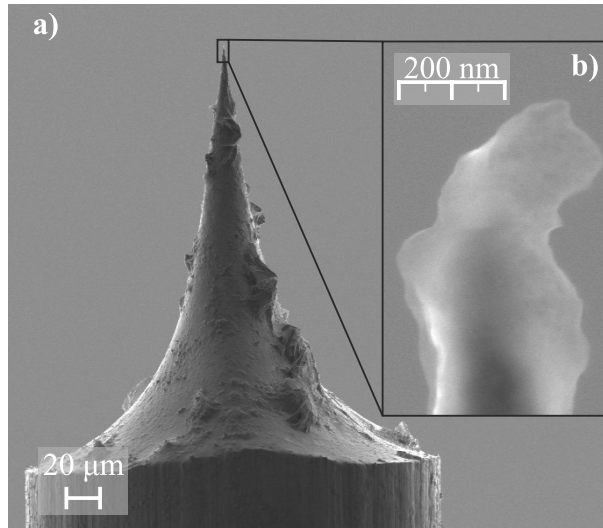


Figure 2.14: SEM images of freshly prepared W STM tip, taken at an acceleration voltage of 5 kV. **a)** 524-times magnification of polycrystalline W wire with a diameter of 0.25 mm that was etched in 5 molar KOH solution. **b)** 200,000-times magnification of black frame in a) shows minimum diameter below 50 nm. These images were taken and adapted from Ref. [54].

As can be seen from Fig. 2.14 b) the minimum diameter of the tip is already below 50 nm. Due to the preparation process, etched W tips are covered by an about 10 nm thick oxide film. If the probe is exposed to in-situ electron bombardment or ion sputtering, the local energy input leads to the removal of the oxide molecules and a further reduction of the tip diameter [69]. Additional voltage pulses during STM in operation can help to remove adatoms at the very end of the probe. For the electro-chemical preparation of the metallic tips different designs can be used, where one example is shown in Fig. 2.15.

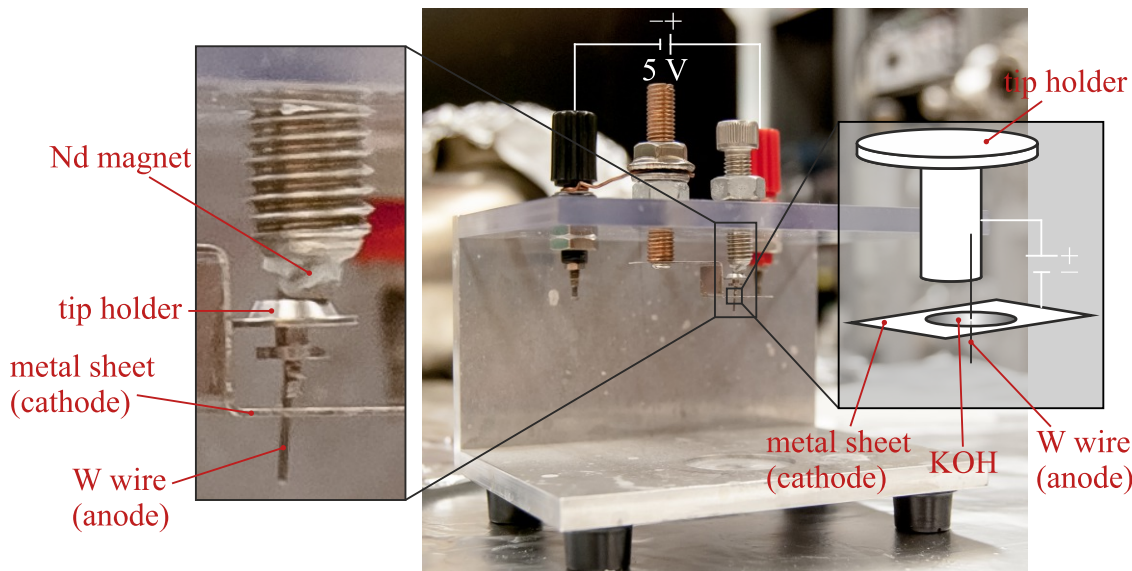
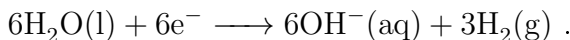


Figure 2.15: Device for electro-chemical preparation of metal tips, which is used at UTK. Magnified inset on the left shows that a Nd magnet, glued to a screw, holds the tip holder. Metal sheet acts as cathode, W wire as anode. If a drop of KOH solution is added, voltage of around 5 V between the electrodes will lead to a current. The less KOH is added, the better defined the area of the etching process will be.

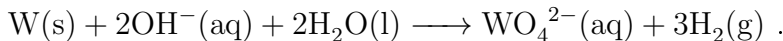
Such an apparatus is based on an electrolytic redox reaction. A piece of W wire is spot-welded to a tip holder and used as anode material. The cathode is a thin sheet of stainless steel with a hole in it, where the wire is put through. If KOH solution is added and a voltage of around 5 V is applied between the electrodes, the following oxidation reaction can be observed at the anode:



Where the W wire comes into contact with KOH, more and more of it is removed while the current is flowing between the two electrodes. The thinner the layer of basic solution, the better defined (future) STM tips will turn out. Several attempts might be necessary to apply the right amount of KOH and the usage of a pipette can be beneficial to remove the surplus solution from underneath. The reduction near the cathode leads to the production of molecular hydrogen:



Everything can be summed up in the total chemical equation:



At some point of the etching process, the wire becomes so thin that the part underneath the KOH layer drops to the ground. Afterward, the tip is cleaned with deionized water from remaining KOH to completely stop the reaction. The appearance, homogeneity, and sharpness of etched probes typically is superior over cut wire pieces, as it is shown for W in Ref. [54]. In STM theory (cf. Sec. 2.3.2) it is assumed that just one single tip atom attributes to the tunneling process. However, the previously discussed influences still have a large impact on the imaging quality and some of them can change during STM in operation, e.g. the constellation of the foremost tip atoms. Therefore, no general conclusions should be drawn from SEM images of the apex shape alone, in particular when these are obtained ex-situ. Although in some experiments the tip quality is examined via in-situ Field-Ion Microscopy (FIM), the real structure while scanning over sample surfaces can not be determined with certainty [49, 70]. It even has been shown that the electronic surface interaction during STM is not just sensitive to the foremost atoms but to the orientation of the foremost orbitals, e.g. during Scanning Probe Microscopy (SPM) with C₆₀ molecules on Si surfaces [71, 72].

2.4.3 Experimental setup

At Universität Osnabrück (UOS) a commercial setup from SPECS SURFACE NANO ANALYSIS GMBH, STM type *Aarhus 150 SPM*, is used. It is integrated in an UHV chamber with five sections: Samples are loaded into the system via load-lock, which reaches p_{pre}^{UOS} ≈ 5 · 10⁻⁸ mbar. Two chambers can be used for different MBE experiments, which both have base pressures around p_{MBE}^{UOS} ≈ 1 · 10⁻⁸ mbar. One of the MBE extensions is equipped with a RHEED setup, allowing experiments with the intensity oscillation technique during film growth. A forth chamber can be used for LEED and

X-ray Photoelectron Spectroscopy (XPS) measurements ($p_{\text{XPS}}^{\text{UOS}} \approx 1 \cdot 10^{-11} \text{ mbar}$). The fifth section of the UHV chamber is equipped with the STM setup mentioned above and reaches base pressures $p_{\text{STM}}^{\text{UOS}} \lesssim 5 \cdot 10^{-10} \text{ mbar}$. Furthermore, a sample garage can be found here, which allows to store several specimen. The samples are moved between the experimental techniques in these sections by several magnetically guided transfer rods that are mounted to the chamber. All sections are individually pumped and separated by gate valves. A schematic illustration is shown in Fig. 2.16 a).

The STM base is built from an aluminium (Al) block, which is attached to four springs and several strings of synthetic rubber. Both the inertia of the metal block as well as the resonant frequencies of the springs and strings are optimized for the best possible damping of oscillations and vibrations. In addition to that, the scanner head is electrically and thermally isolated against the metal block by three quartz crystal balls. The STM head combines two drives, as it was already mentioned in Sec. 2.4.1. For the fine x-, y-, and z-movements of the tip a single piezo-electric tube is used, while the (relatively coarse) approach movement of the STM head is realized by an inchworm motor. A cross-sectional view of the *Aarhus 150 SPM* design is given in Fig. 2.16 b).

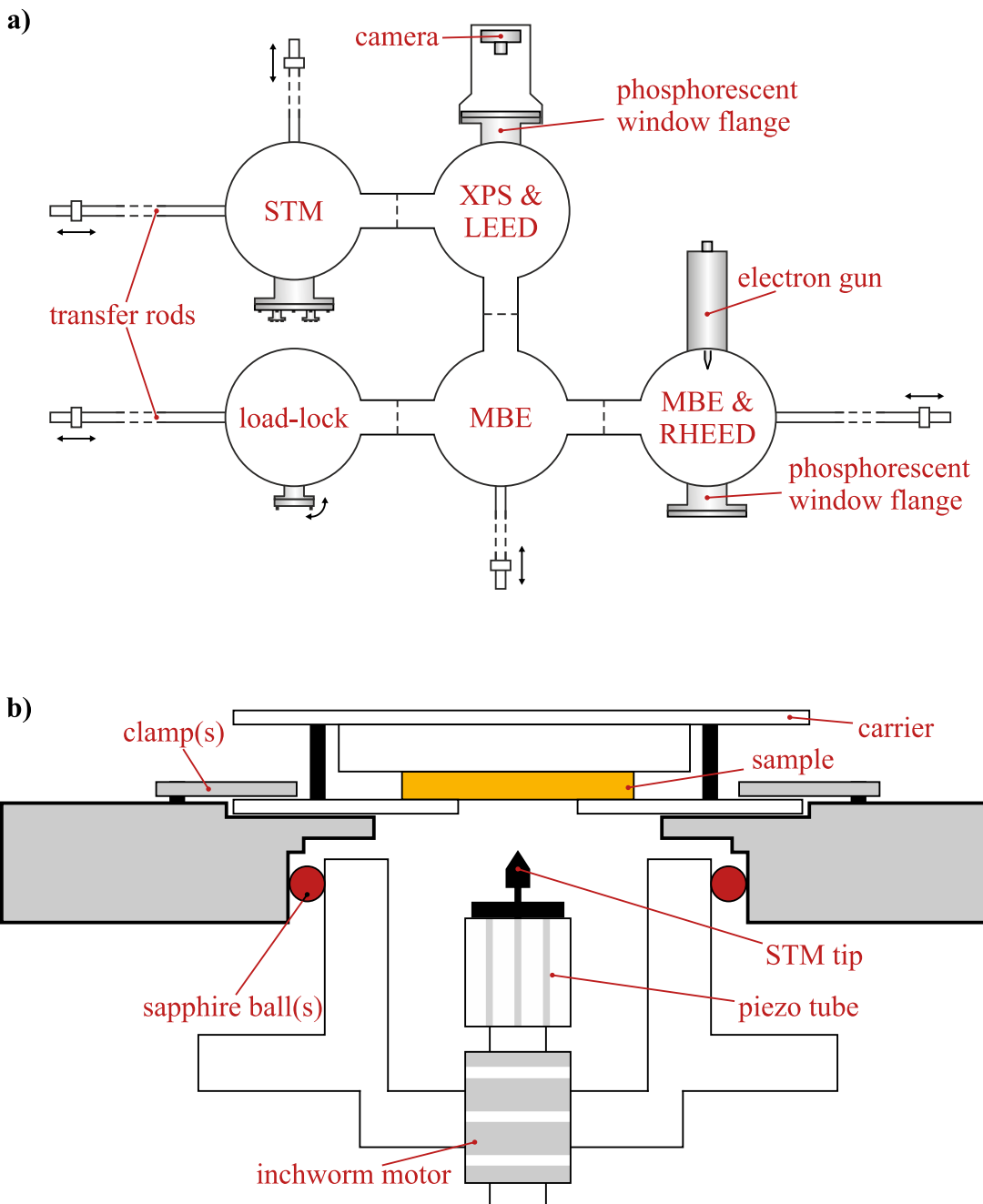


Figure 2.16: UHV chamber and STM setup at UOS. **a)** Schematic top view of UHV chamber at UOS, which consists of five sections: Samples are loaded into UHV via load-lock. MBE can be realized in two chambers, one in combination with a RHEED setup. Another section allows LEED and XPS measurements (hemispherical analyzer not shown, but would be orthogonal to this illustration). All sections are individually pumped and separated by gate valves. Transfer rods can be used for sample movement and a garage in the STM section allows storage of several samples. **b)** Schematic cross-section of STM type *Aarhus 150 SPM* by SPECS SURFACE NANO ANALYSIS GMBH. The x-, y-, and z-movements of the tip are realized by a piezo-electric tube, while an inchworm motor is used for coarse approach movements.

3 Investigated materials

3.1 Si

The element Si has the atomic number $Z = 14$ and is a tetravalent semiconductor. It is placed in the fourth main group and third period of the periodic table of elements. Besides, it exhibits a melting point of 1414°C and crystallizes in the diamond structure for temperatures lower than this. The crystal structure is equivalent to a non-primitive face centered cubic (fcc) lattice with a basis containing two atoms at the lattice positions $(0\ 0\ 0)$ and $(\frac{1}{4}\ \frac{1}{4}\ \frac{1}{4})$. The lattice constant of the cubic Si unit cell is $a_{\text{Si}} = 5.431\text{\AA}$. A schematic illustration of the diamond cubic crystal structure is shown in Fig. 3.1.

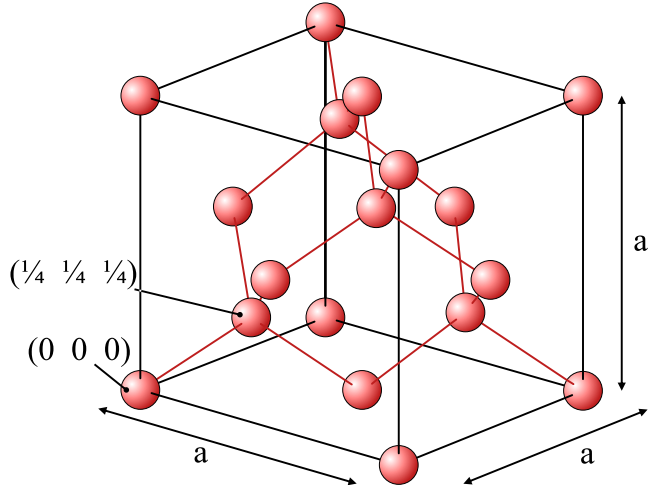


Figure 3.1: Diamond cubic crystal structure of Si, which is equivalent to a non-primitive fcc lattice with a basis containing two atoms at the lattice positions $(0\ 0\ 0)$ and $(\frac{1}{4}\ \frac{1}{4}\ \frac{1}{4})$. The lattice constant is $a = 5.431\text{\AA}$. This image was taken and adapted from Ref. [73].

Elemental Si of highest purity is widely used in nowadays semiconductor electronics, e.g. it may be found as substrate of integrated circuits in almost every modern device. It offers relatively good accessibility and low costs (second most common element in the Earth's crust [74]) in combination with tunable electrical properties. However, most of it is distributed in the form of oxides or silicates but finds usage in biology, materials science, and chemistry without being separated. The electrical properties of pure Si can be manipulated by doping with other elements, e.g. phosphorus (P) or boron (B). Through this the charge carrier concentration and therefore the properties are changed by replacing Si atoms at distinct lattice positions.

The unreconstructed Si(100) surface exhibits a simple cubic (sc) surface unit cell with the lattice constant $a = a_{\text{Si}}/\sqrt{2} = 3.84\text{\AA}$ and layer distance $d = a_{\text{Si}}/4 = 1.36\text{\AA}$, resulting from the diamond cubic crystal structure (cf. Fig. 3.1). After the usual temperature treatment, which will be extensively introduced in Sec. 4.1, a $(2 \times 1)/(1 \times 2)$ -reconstruction can be observed on Si(100) surfaces [14]. This is sketched in Fig. 3.2.

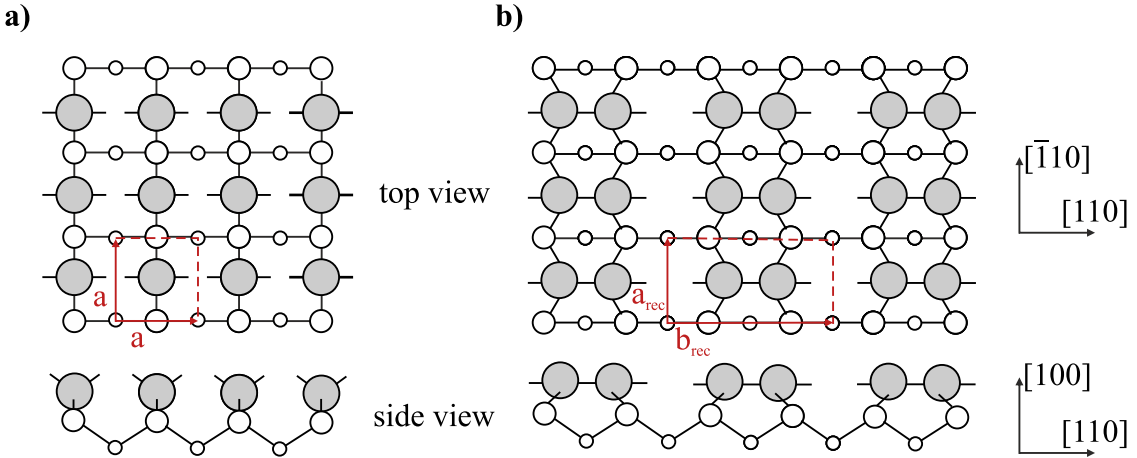
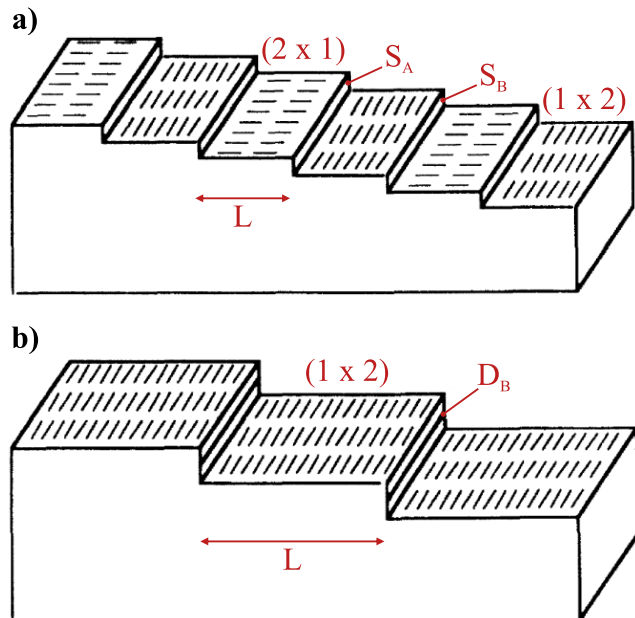


Figure 3.2: Si(100) surface with **a)** bulk-terminated (1×1) -lattice and **b)** (2×1) -reconstruction. The unsaturated bonds of the topmost atoms (sketched in gray) favor the formation of dimers, which leads to a larger unit cell given by $a_{\text{rec}} = a = 3.84 \text{ \AA}$ and $b_{\text{rec}} = 2 \cdot a = 7.68 \text{ \AA}$. This image was taken and adapted from Ref. [14].

As can be seen from this image, each of the topmost Si atoms is bonded to two atoms of the next lower layer. Hence, each surface atom features two dangling bonds and the formation of dimers is favored saturating half of those [75]. Atoms at terrace edges are rebonded and form dimer-like bonds with lower terrace atoms [76]. As a result of this behavior and the underlying diamond structure (cf. Fig. 3.1), the orientation of the dimer rows changes by 90° on neighboring terraces that are separated by single-layer step height. Although this is valid for any kind of Si(100) surface, a schematic illustration of the dimer orientation shifting on a vicinal surface is shown in Fig. 3.3.

Figure 3.3: Vicinal Si(100) surface showing **a)** single-layer step height with two and **b)** double-layer step height with just one of the two surface reconstructions. The resulting step edges are indicated by S_A , S_B , and D_B , respectively. In accordance to Eq. (2.12) the angle of vicinality is associated with terrace width and layer distance by $\tan(\vartheta_c) = \frac{d}{L}$. This image was taken and adapted from Ref. [77].



The terrace type with the dimer rows parallel to the step edge will be labeled as (2×1) -, the other one as (1×2) -reconstruction in the following. The ratio of both

can be manipulated by different parameters, e.g. the applied direct current (DC) direction or the mean angle of vicinality [78–83]. Under the assumption of exclusively double-steps between neighboring terraces, one can expect an average terrace width $L = 3.89 \text{ nm}$ for $d = 1.36 \text{ \AA}$ and $\vartheta_c = 4^\circ$ (cf. Eq. (2.12)). Anyhow, in Ref. [14] it is shown that the regular constellation in Fig. 3.2 b) is just the frozen image of a dynamic and random dimer buckling. Since this motion appears on a shorter time scale than the investigating methods, e.g. STM or LEED, are able to resolve, only time-averaged images can be gained from Si(100) surfaces at room temperature (RT). This, however, changes at temperatures below 200 K and with decreasing temperature more and more asymmetric dimers become visible.

The samples investigated during this thesis were cut from vicinal p-type Si(100)-wafers. These were slightly B-doped so that they offer a specific resistance between $1 \Omega \text{ cm} > \sigma > 20 \Omega \text{ cm}$. Their thickness is given by $525 \mu\text{m}$ and the angle of vicinality by $\vartheta_c = 4^\circ$ towards $\langle 110 \rangle$. A schematic illustration of such a wafer can be found in Fig. 3.4. Here, the (imaginary) direction of the step edges on the surface is indicated by dashed lines and the angle of vicinality by ϑ_c .

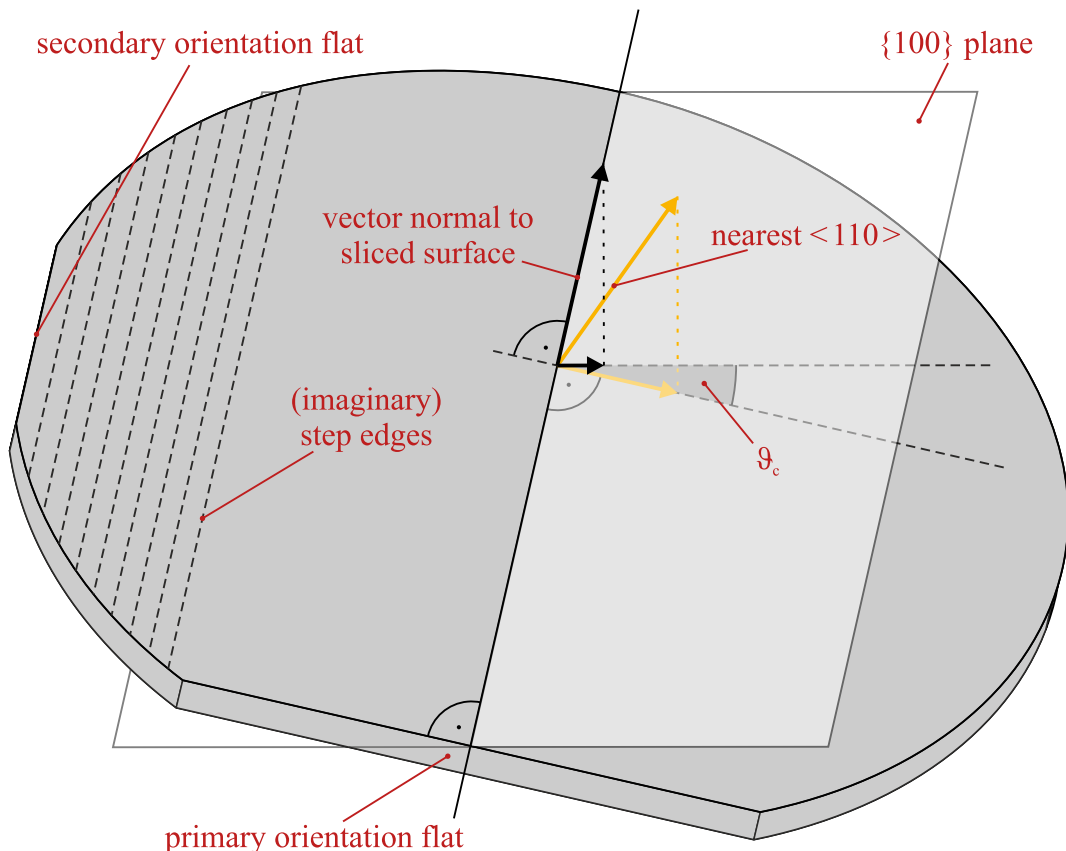


Figure 3.4: Schematic illustration of an industrial Si(100)-wafer with 4° miscut towards $\langle 110 \rangle$. Primary and secondary flats indicate a $\{100\}$ -surface of p-type. The direction of the step edges on the surface is indicated by dashed lines and the angle of vicinality is given by ϑ_c .

3.2 Y and its silicides

The element yttrium (Y) has the atomic number $Z = 39$ and may be found in the third subgroup and fifth period of the periodic table of elements. It is a trivalent transition metal showing chemical properties very similar to the lanthanides and is often classified as one of the rare earth elements (REE). It crystallizes in the hexagonal closed-package (hcp) structure and reveals the lattice parameters $a_Y = 3.6474 \text{ \AA}$ and $c_Y = 5.7306 \text{ \AA}$ and shows a melting point of 1523°C [84]. In nature Y is never found in its elemental form but often in compounds with other REE. The production of highly purified Y is relatively complex and expensive, since it is difficult to separate REE from each other and the earthly Y amount is only 31 ppm in total.

If Y is deposited on Si at elevated temperatures, silicide formation has to be considered. With regard to possible nanophases, this process in general is very sensitive to the evaporating conditions. For instance, an Y-induced (2×7) -reconstruction appears on Si(100) surfaces due to wetting layer formation for low coverages and relatively low temperatures [1]. The growth of the wetting layer is a well-known phenomenon for several REE silicides on Si(100) surfaces [85–87]. It is, however, limited by a coverage of about 0.35 ML, since this represents a surface that is completely covered by the (2×7) -reconstruction. The exact structure and origin of the wetting layer has not been clarified yet.

On top of the surface reconstruction nanowire growth sets in. Regarding this, it remains unclear, whether the orientation of the nanowires relative to the dimers of the reconstructed Si(100) $(2 \times 1)/(1 \times 2)$ -surface are induced or otherwise affected by the formation of a wetting layer [1]. Anyhow, for relatively thin RESN it is known that they crystallize in the hexagonal AlB_2 -structure, leading to the stoichiometry YSi_2 in this case [86]. The schematic illustration of a bulk unit cell can be found in Fig. 3.5.

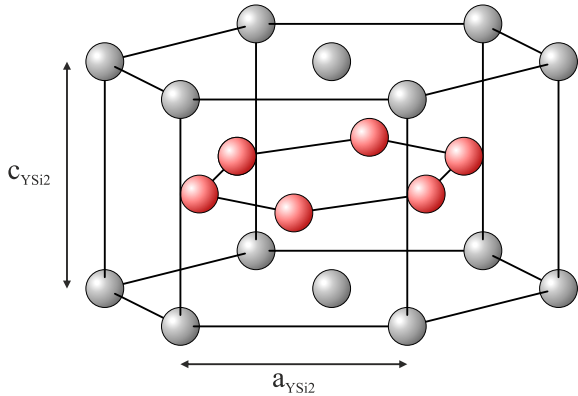


Figure 3.5: The bulk-terminated unit cell of YSi_2 exhibits the hexagonal AlB_2 -structure and contains of three Y atoms (grey) and six Si atoms (red). The lattice constants are given by $a_{\text{YSi}2} = 3.842 \text{ \AA}$ and $c_{\text{YSi}2} = 4.144 \text{ \AA}$.

Here, the lattice constants are given by $a_{\text{YSi}2} = 3.842 \text{ \AA}$ and $c_{\text{YSi}2} = 4.144 \text{ \AA}$. Therefore, YSi_2 perfectly matches the lattice constant a_{rec} of the reconstructed Si(100) surface in $\langle\bar{1}\bar{1}0\rangle/\langle1\bar{1}0\rangle$ -direction (cf. Fig. 3.1). Due to the high lattice mismatch along b_{rec} , the growth of crystalline structures along the $\langle110\rangle/\langle\bar{1}\bar{1}0\rangle$ -direction is prohibited and leads to uni-directional growth of atomic wires. ZENG et al. performed calculations using density functional theory (DFT) on the surface DoS of YSi_2 -nanowires [86]. In particular, they solved the structural and electronic properties of wires with a three

times larger width than the lattice constant a_{rec} . A cross-sectional and a side view of the surface structure confirmed by them is given in Fig. 3.6.

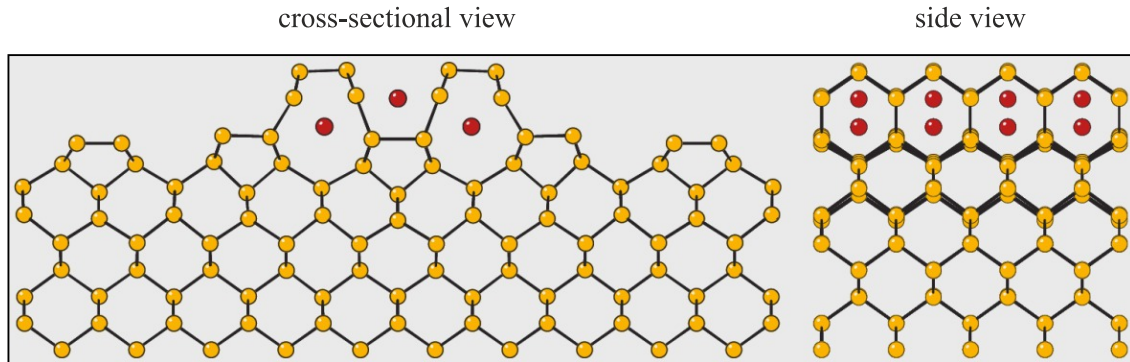


Figure 3.6: Cross-sectional and side view of YSi_2 surface unit cells from DFT-calculations. The nanowires exhibit a three times larger width than the lattice constant a_{rec} of the underlying $\text{Si}(100)$. Here, Y atoms are shown in red and Si atoms in yellow. This image was taken and adapted from Ref. [86].

4 Results and discussion

In this thesis, Si substrates with (100) surface orientation and 4° miscut towards $\langle 110 \rangle$ were used. They will be referred to as vicinal Si(100) substrates in the following for simplificational reasons. A few results for comparing purposes were also obtained from nominally flat Si(100) surfaces. All samples were characterized with RHEED and STM, which have been introduced as experimental techniques in Chap. 2. The diffraction patterns obtained from RHEED are manipulated for a better visibility of weak features and should not be used for quantitative conclusions, except stated otherwise.

4.1 Substrate preparation

A first move towards the epitaxial growth of YSi_2 -nanowires on vicinal Si(100) surfaces is the substrate preparation and characterization. It is common practice to clean Si samples by DC heating. Here, the surface quality can be influenced by several parameters, e.g. the flash-heating temperature, DC direction, and post-annealing (PA) procedure. The goal of this work is to investigate the growth of ordered YSi_2 -nanowire arrays on vicinal Si(100) surfaces. Hence, the underlying substrate should fulfill the following criteria:

- 1) (1×2) -reconstruction at the surface (cf. Fig. 3.3).
- 2) Homogenously distributed terrace width L.
- 3) Si dimer rows without vacancies (cf. Fig. 3.2).

The first aspect is motivated by the fact that RESN in general run perpendicular to the dimer rows and were meant to grow along the terrace edges. Hence, (1×2) -terraces are necessary for a growth that is not immediately limited by the step edges. As can be seen in Sec. 3.1 this is automatically fulfilled for surfaces, where the terraces are separated by parallel edges with double-step height. If the second criterion is satisfied, the Si substrate governs the inter-wire distance of the YSi_2 -nanowires in terms of the average terrace width. Furthermore, the dimer rows should not exhibit any defects or vacancies, since these represent the building foundation of the silicides.

The first step of sample preparation was cutting them from industrial Si wafers. Afterward, the substrates were marked with a dot on the backside so that the crystallographic axes could be tracked over the whole procedure. Subsequently, they were cleaned in an ultrasonic bath for approx. 10 min each in acetone and isopropyl alcohol. After bringing them into the load-lock and pumping down the pre-chamber, the samples were degassed for several hours at $T_{\text{sam}} \approx 450^\circ\text{C}$ until the UHV system reached

base pressure ($p_{\text{main}}^{\text{UTK}} \approx 3 \cdot 10^{-11} \text{ mbar}$) again. The degassing was achieved with a pyrolytic boron nitride (PBN) crystal at UTK, while similar results were gained with DC heating of the samples themselves at UOS. The PBN crystal is integrated in the manipulator right behind the sample holder and has the disadvantage that it heats up several components in the immediate vicinity. Due to the fact that the sample stage is hundreds of degrees cooler than the PBN crystal, condensation may appear. But good results were obtained, since the environment of the sample stage was relatively clean. This is supported by the fact, that the main chamber only rises to a pressure of $p_{\text{PBN}}^{\text{UTK}} \approx 5 \cdot 10^{-10} \text{ mbar}$ during the annealing process. In the contrary, the samples are the hottest point when they are degassed with DC heating. However, poor contacts between clamps and samples may be a drawback, since the contact properties often change with temperature as the samples change their volume.

At the very beginning, the influence of the flash-heating temperature was investigated without regard to the other parameters. However, these were kept as constant as possible for all specimen. The Si samples were flash-heated several times until the pressure did not rise over $p_{\text{max}} = 1 \cdot 10^{-9} \text{ mbar}$ for at least 20 s. Then, the surfaces were assumed to be clean and the increasing pressure was attributed to the up-heating surroundings. In consistency with the literature [88–94, and references therein], 1250 °C was found to lead to clean surfaces, while it is still relatively far away from the Si melting point. Even in hot spots, which always tend to appear when clamps are used as contacts, this temperature does not lead to melted sites. An infrared pyrometer with a precision of $\pm 25^\circ\text{C}$ was used to determine the sample temperatures. The flashing procedure is mainly based on the results presented in Ref. [94]. The established recipe for the preparation of Si(557) (vicinal Si(111)) was optimized for vicinal Si(100) surfaces here. After finding the optimum temperature, the preparation procedure was investigated concerning a possible influence from the DC direction [78–83, 95–98].

A STM image of the vicinal Si(100) surface, which was flash-heated with an applied DC down the staircase, is shown in Fig. 4.1.

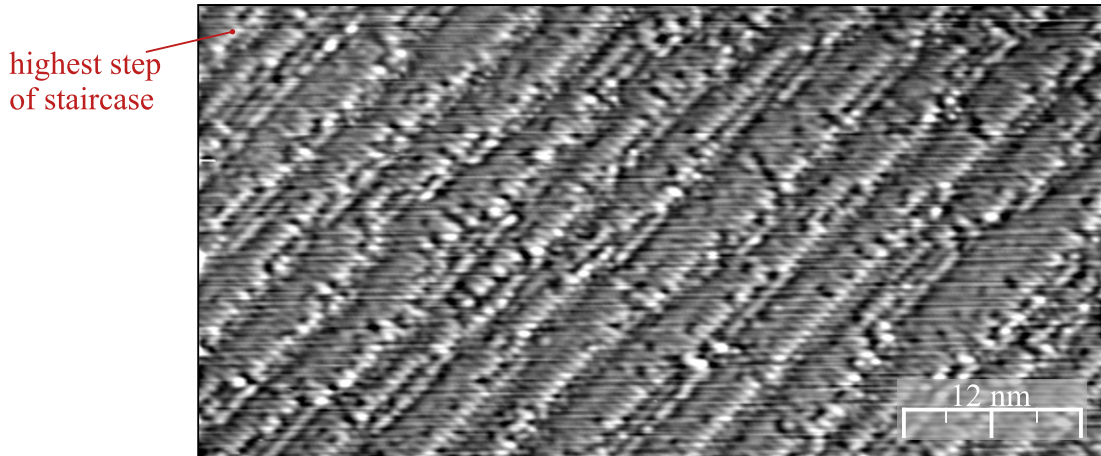


Figure 4.1: STM image (CCM, $V_T = -1.5 \text{ V}$, $J_{\text{set}} = 0.07 \text{ nA}$) of vicinal Si(100) surface that was flashed multiple times at 1250 °C with DC heating step-down, quenched to RT with tens of degrees per second, and not post-annealed.

In this image a general tendency of the surface to form double steps can be observed, which is not surprising at this off-axis angle according Ref. [83]. Besides, the predominant terrace type is the (1×2) -reconstruction, which is assumed to originate from the slightly lower surface energy at step edges [99–101]. If a vicinal Si(100) surface is prepared as explained above, it exhibits terraces that are almost equal in their widths. However, in contrast to the quality criteria defined at the beginning of this section, some terraces appear where the dimer rows run parallel to the step edges. Furthermore, the dimer rows themselves show a lot of vacancies affecting the overall surface roughness. In order to eliminate the observed dimer defects and potentially increase the surface coverage by (1×2) -terraces, the same sample was flash-heated again a few times. But in opposition to the previous procedure it was quenched to 935°C within 30 s after the last flashing (cf. Ref. [94]). At these conditions, it was kept for 15 min in terms of PA and subsequently cooled to RT with a rate of $< 1^\circ\text{C}/\text{s}$. A STM image of this vicinal Si(100) surface can be found in Fig. 4.2.

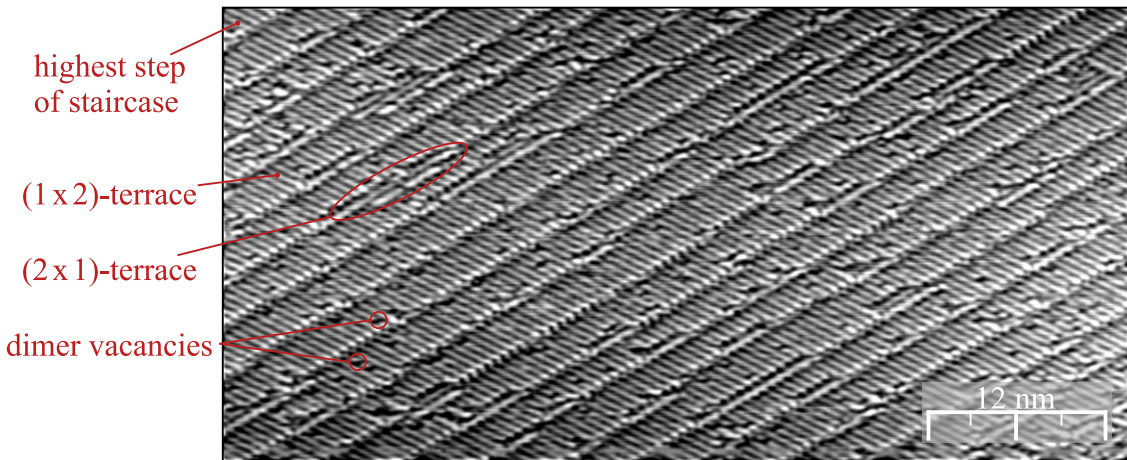


Figure 4.2: STM image (CCM, $V_T = -1.5\text{ V}$, $J_{\text{set}} = 0.1\text{ nA}$) of vicinal Si(100) surface, which was flash-heated multiple times at 1250°C with applied DC in step-down direction and was quenched to 935°C within 30 s. At this temperature, PA was performed for 15 min, followed by cooling down to RT with a rate of $< 1^\circ\text{C}/\text{s}$.

The additional PA treatment obviously leads to the formation of smoother terraces in comparison to Fig. 4.1. The majority of them is separated by double steps, but some parts of the surface also exhibit terraces with single-layer step height (cf. Sec. 3.1). These are covered by the (2×1) -reconstruction that can be seen as dimer rows running step-parallel. The overall appearance of this sample's surface exhibits parallel step edges with very few kinks. Anyhow, one can still observe dimer vacancies, which were meant to be eliminated by the PA. As these might be suspected to be a remaining feature from the previous treatment, a completely new specimen was cut and brought into UHV. This sample was only exposed to the second preparation procedure, which lead to the very same results as noticed in Fig. 4.2.

Subsequently, another sample was cut, cleaned, and degassed in UHV like described before. Compared to the surface in Fig. 4.1 the preparation parameters were the same, except for the current direction. This sample was flash-heated with an applied

DC step-up and therefore in the opposing direction as displayed in Fig. 4.1. The STM image corresponding to this surface is shown in Fig. 4.3.

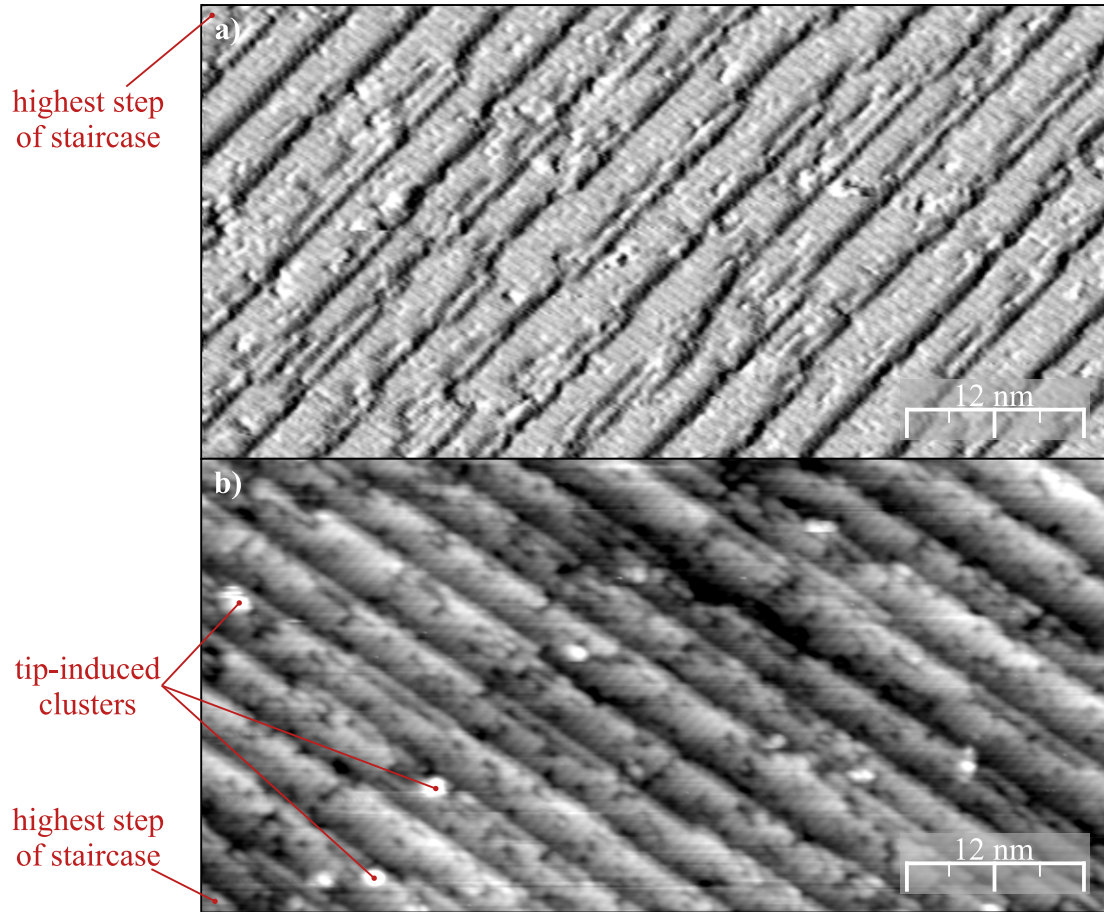


Figure 4.3: STM images (CCM, $V_T = -2.0$ V, $J_{set} = 0.1$ nA) of vicinal Si(100) surface that was flashed multiple times at 1250 °C with DC heating step-up, quenched to RT with tens of degrees per second, and not post-annealed. **a)** Derivative topography to increase the visibility of (differentiated) height information from the sample over static noise. This part of the surface shows a lot of kinks and terraces, which are separated by single steps, but mostly defect-free dimer rows. **b)** Other surface regions exhibit more parallel step edges with fewer kinks, but the dimer rows reveal vacancies here.

This preparation procedure leads to a volatile surface structure. On the one hand, regions with almost entirely defect-free dimer rows can be found. However, these are accompanied by a lot of terraces with single-layer step height and therefore both surface reconstructions (cf. Fig. 4.3 a)). The appearance of many kinks along the step edges creates the impression of a very rough surface. On the other hand, some parts of the surface exhibit mostly parallel step edges with just a few kinks and therefore not so many single steps (cf. Fig. 4.3 b)). These are predominantly covered by the (1 × 2)-reconstruction but reveal a lot of dimer vacancies at the same time. Hence, this vicinal Si(100) surface was not considered to be an ideal substrate for the growth

of YSi_2 -nanowires either³. In consistency with the two previous samples (cf. Fig. 4.1 and Fig. 4.2) a PA procedure was added to the preparation process of this substrate. The preparation conditions of the sample surface in Fig. 4.4, hence, are identical to those in Fig. 4.2, except for the opposing direction of the applied DC.

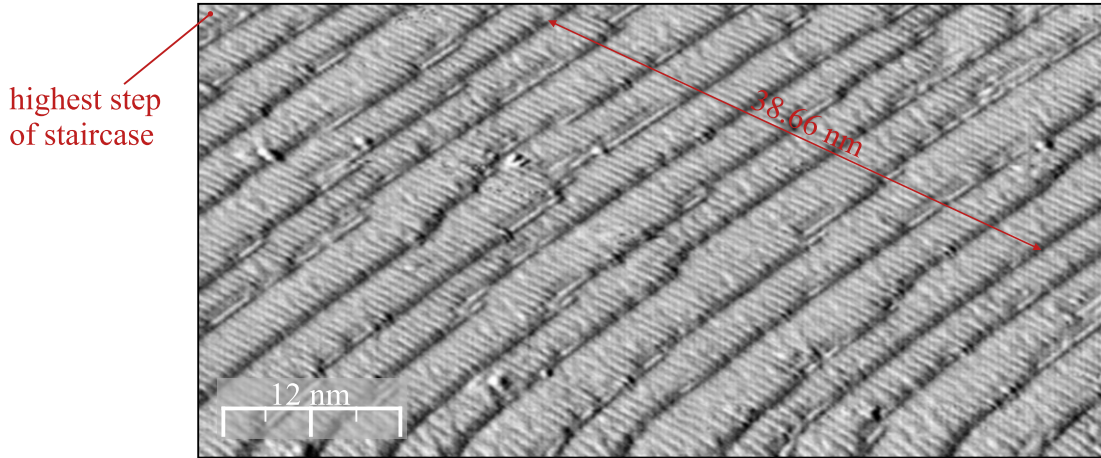


Figure 4.4: STM image (CCM, $V_T = -1.5 \text{ V}$, $J_{\text{set}} = 0.1 \text{ nA}$) of the derivative topography of a vicinal $\text{Si}(100)$ surface, which was flash-heated at 1250°C with applied DC in step-up direction and quenched to 935°C within 30 s. At this temperature, PA was performed for 15 min, followed by cooling down to RT with a rate of $< 1^\circ\text{C}/\text{s}$.

The height profile across the terraces in the upper right of this image (red solid line) can be found in Fig. 4.5.

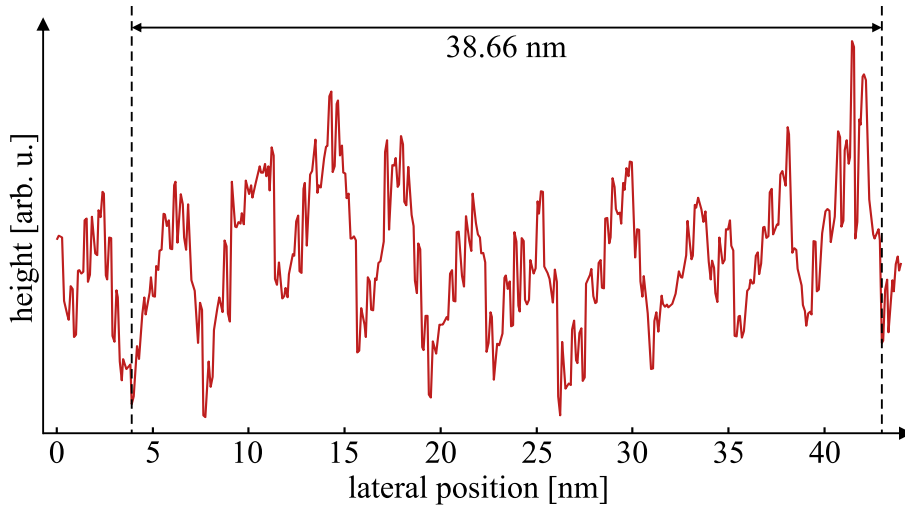


Figure 4.5: Height profile along the red solid line in Fig. 4.4. Note that the STM image already was flattened. The average terrace width, however, can be determined to be $L_{\text{exp}} \approx 3.87 \text{ nm}$, which is very close to $L_{\text{calc}} \approx 3.89 \text{ nm}$ (cf. Sec. 3.1).

³ The white spots in Fig. 4.3 b) are not attributed to structures of the $\text{Si}(100)$ surface but just small clusters that are deposited by the STM tip from time to time.

According to the line scan in Fig. 4.5, the mean terrace size can be determined to $L_{\text{exp}} \approx 3.87 \text{ nm}$. Thus, the surface shows the kind of terraces, which are expected for $\vartheta_c = 4^\circ$ and separated by double steps (cf. Sec. 3.1). Although Fig. 4.4 shows a derivative topography image in order to suppress static noise, it can be clearly seen how smooth the surface is. It exhibits almost exclusively terraces with (1×2) -reconstruction at the surface. The mostly parallel step edges are interrupted by very few kinks, which are often accompanied by small (2×1) -domains. These cover approx. 7.5 % of the surface. The coverage by terraces with the major (1×2) -reconstruction and the overall surface quality were verified at different sample positions. Hence, the surface structure does not seem to be as volatile as it was observed for the sample in Fig. 4.3. Furthermore, the dimer rows in this image reveal no (and on a large scale only very few) vacancies, which is why the preparation procedure with DC in step-up direction and PA is considered the best yet.

To check if the surfaces can become even more suitable for nanowire growth, the surface preparation was repeated with a completely new sample. Fig. 4.6 shows the STM image of a vicinal Si(100) surface, where the DC was applied in step-parallel direction.

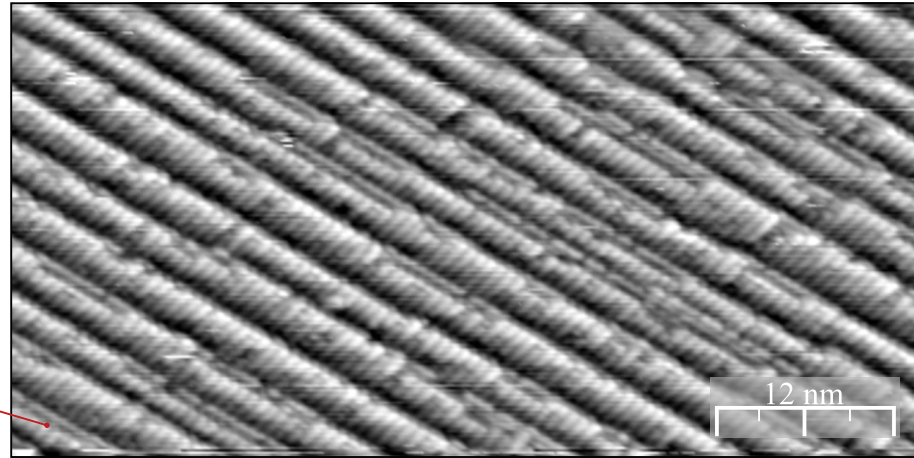


Figure 4.6: STM image (CCM, $V_T = -1.5 \text{ V}$, $J_{\text{set}} = 0.1 \text{ nA}$) of vicinal Si(100) surface that was flashed multiple times at 1250°C with DC heating step-parallel, quenched to RT with tens of degrees per second, and not post-annealed.

From this image it can be seen that flash-heating with step-parallel DC leads to even less kinks than for the preparation parameters in Fig. 4.4. Therefore, very straight and parallel step edges can be observed and the overall surface exhibits a low roughness, which may be associated with the increased electromobility when the current flows along the step edges [95, 96]. However, mostly (1×2) -terraces are obtained at the surface but the amount of those with a (2×1) -reconstruction is significantly higher than before (approx. 18.1 %). Furthermore, the dimer rows reveal a relatively high defect density compared to the surface in Fig. 4.4. In order to achieve dimer rows with less vacancies and to complete this series of sample preparations, the same sample was flash-heated a few more times and subsequently PA was performed. A STM image of the resulting Si(100) surface can be seen in Fig. 4.7.

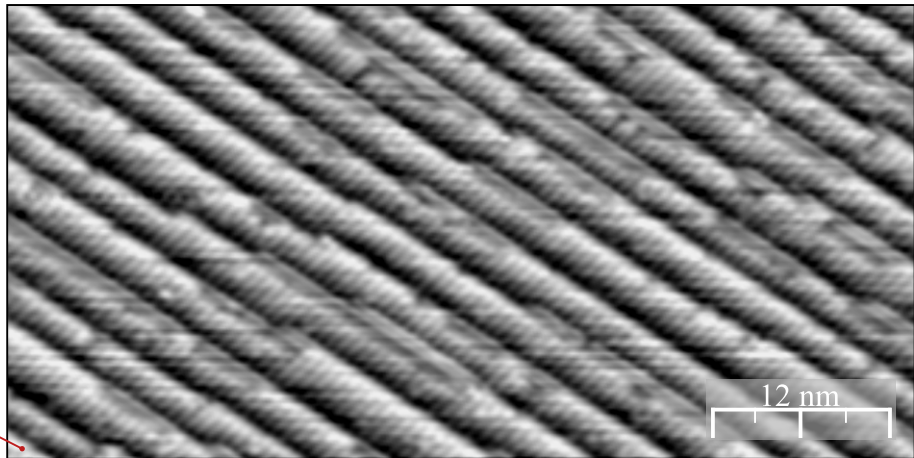


Figure 4.7: STM image (CCM, $V_T = -1.5$ V, $J_{\text{set}} = 0.05$ nA) of vicinal Si(100) surface, which was flash-heated multiple times at 1250°C with applied DC in step-parallel direction and quenched to 935°C within 30 s. At this temperature, PA was performed for 15 min, followed by cooling down to RT with a rate of $< 1^\circ\text{C}/\text{s}$.

Apparently, the additional PA procedure does not have as much effect on the surface quality as it was observed for the samples with an applied DC perpendicular to the steps. In comparison with the only flash-heated sample in Fig. 4.6, the terraces reveal a similar amount of kinks and (2×1) -domains. Again, the step edges run mostly parallel to each other, while the terrace widths are homogeneously distributed. Although still existent, the surface in Fig. 4.7 shows less dimer vacancies than the sample that was just flash-heated and quenched without subsequent PA. After the last temperature treatment Y was deposited on this sample as is. The sample temperature during deposition was $T_{\text{dep}} \approx 625^\circ\text{C}$, the evaporating time $t_{\text{evap}} = 60$ s, and the evaporating power $P_{\text{evap}} \approx 39.9$ W. The sample was quenched to RT at the same time the shutter of the evaporator was closed. Fig. 4.8 shows a STM image of the resulting surface.

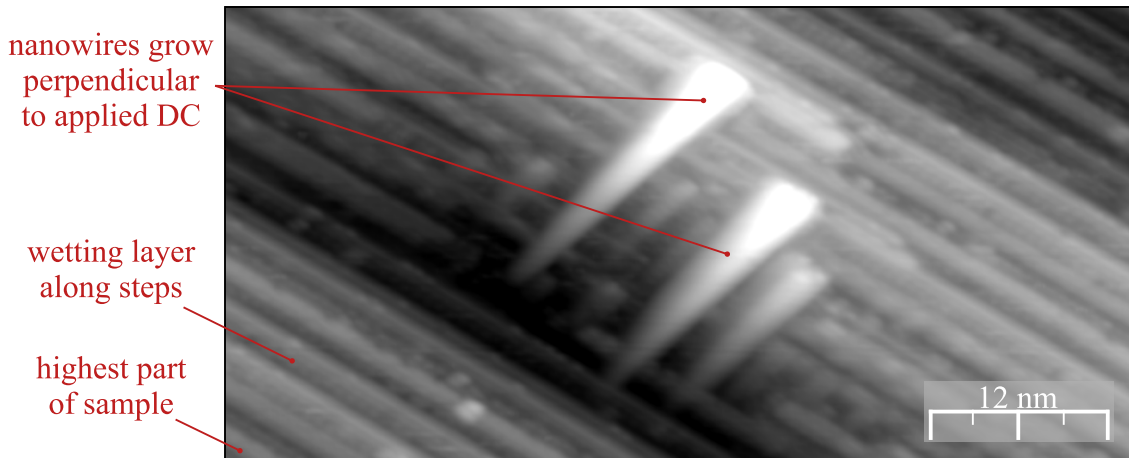


Figure 4.8: STM image (CCM, $V_T = -1.5$ V, $J_{\text{set}} = 0.1$ nA) of YSi_2 -nanowires on the vicinal Si(100) surface seen in Fig. 4.7. Evaporating parameters: $\theta \approx 0.4$ ML, $T_{\text{dep}} \approx 625^\circ\text{C}$, $t_{\text{evap}} = 60$ s, $P_{\text{evap}} \approx 39.9$ W, no PA after growth.

The Y amount on the surface can be calibrated by the coverage of the wetting layer and was about $\theta \approx 0.4$ ML in this case, since the wetting layer was complete and the first nanowires started forming [1]. As can be seen from Fig. 4.8, a non-negligible part of the surface was occupied by YSi_2 -nanowires growing perpendicular to the step edges (the longest have lengths around 21 nm). The origin of this can not be explained, since this behavior was not observed before on vicinal $\text{Si}(100)$ surfaces. Anyhow, it was considered to be a drawback regarding the task to grow ordered YSi_2 -nanowires along the step edges.

In general, one can conclude that the vicinal $\text{Si}(100)$ surfaces with applied PA procedure are superior concerning the earlier defined criteria over those without PA. This statement includes the surface roughness, quality of dimer rows, and (at least for the step-up flashed samples) coverage by (1×2) -terraces. Considering the surprising result of the nanowire growth in Fig. 4.8, the results concerning an optimized substrate preparation can be summarized in the following list:

- 1)** Cutting sample with step edges perpendicular to its long edge.
- 2)** Applying DC in step-up direction.
- 3)** Flash-heating at 1250°C ($p_{\max} = 1 \cdot 10^{-9}$ mbar).
- 4)** Quenching to 935°C within 30 s.
- 5)** PA at this temperature for 15 min.
- 6)** Cooling down at a rate of $< 1^\circ\text{C}/\text{s}$.

These parameters lead to surfaces, which were found to satisfy the criteria list from the beginning of this section as good as possible. Hence, they were the most suitable for the formation of RESN on vicinal $\text{Si}(100)$ surfaces and in particular were used for the growth of YSi_2 -nanowires. The wire growth will be presented for nominally flat $\text{Si}(100)$ surfaces in Sec. 4.2 and for the vicinal ones in Sec. 4.3.

4.2 YSi_2 on flat $\text{Si}(100)$

In order to get a feel for the preparation in general and to have a reference point for RHEED measurements of the vicinal $\text{Si}(100)$ surfaces, the YSi_2 -nanowires were grown on a nominally flat sample first. Here, the deposition temperature was $T_{\text{dep}} \approx 623^\circ\text{C}$, the evaporating time $t_{\text{evap}} = 70$ s, and the evaporating power $P_{\text{evap}} \approx 39.0$ W. Again, it was arranged to simultaneously quench the sample to RT and close the shutter in front of the evaporator. Thus, the nanowires were not exposed to PA. Diffraction patterns of the clean and silicide-covered surface can be found in Fig. 4.9.

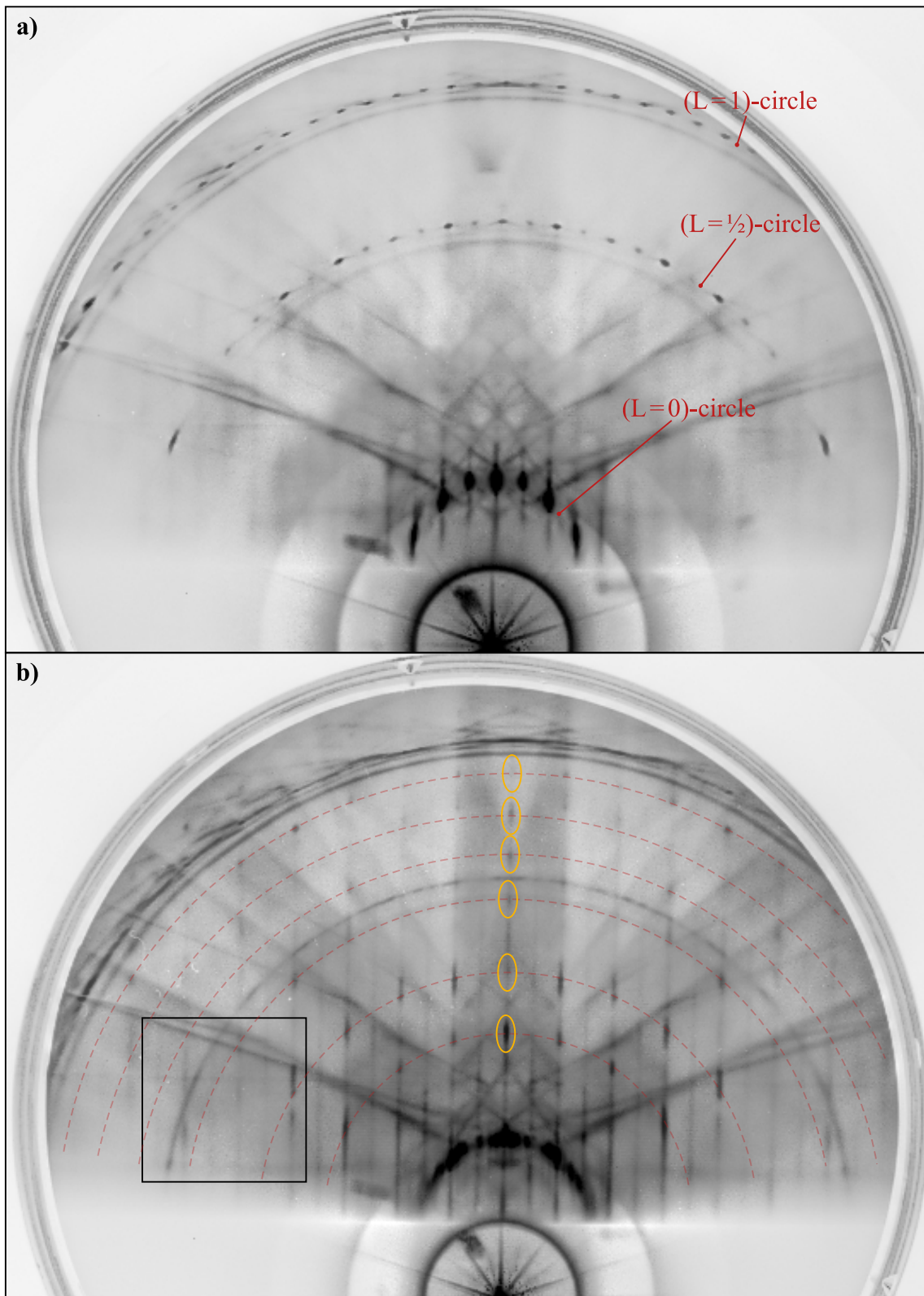


Figure 4.9: RHEED pattern (15 keV, electron beam in $\langle\bar{1}10\rangle/\langle1\bar{1}0\rangle$ direction) of flat Si(100) **a)** as clean surface and **b)** with Y-coverage ($\theta \approx 0.35$ ML). The black frame is shown in Fig. 4.11, while the red, dashed circles indicate additional LAUE-circles.

The basic features of the diffraction pattern in Fig. 4.9 a), i.e. corresponding streaks of the cubic (1×1) -lattice and the $(2 \times 1)/(1 \times 2)$ -superstructure of the reconstructed Si(100) surface, have been explained in Sec. 2.2.1 on the basis of Fig. 2.6. The origin of the additional streaks at the $(\frac{1}{2} \frac{1}{2})$ -position and integer multiples hereof, however, was not clarified yet. Again, it should be noted that the RHEED images shown in Fig. 4.9 were merged from ten single diffraction patterns with different intensities. This was realized by varying the detection time of the used camera and capturing one pattern for each setting. Through this, one obtains an image with extended dynamic range and an increased visibility of weak features, which should not be used for quantitative statements concerning spot intensities. The inverted diffraction pattern from Fig. 4.9 a) without the manipulated dynamics can be seen in Fig. 4.10.

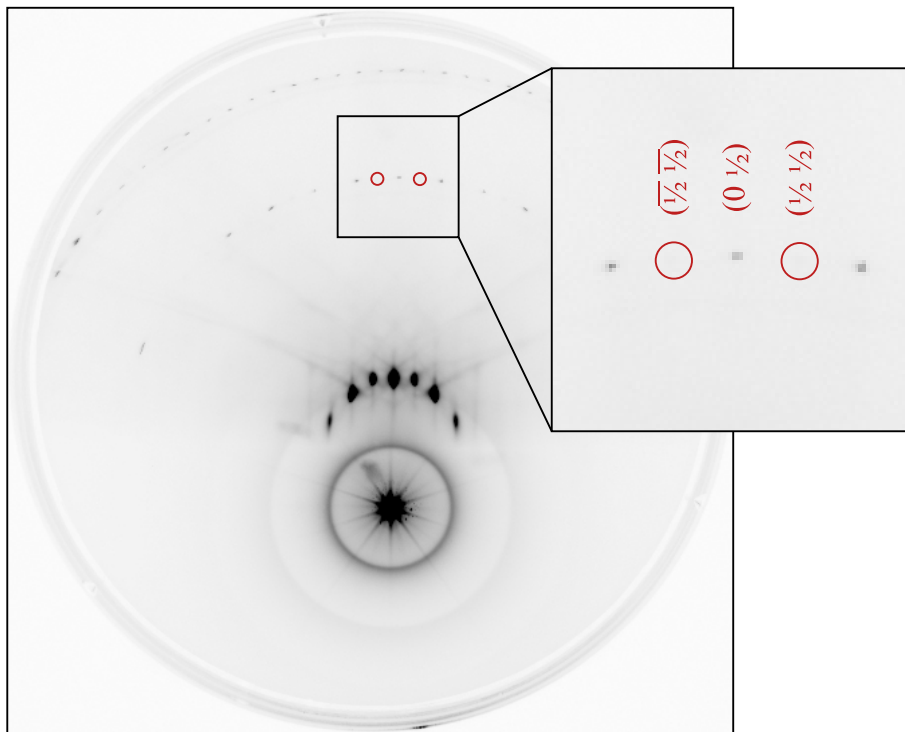


Figure 4.10: Inverted RHEED pattern of the same Si(100) surface as shown in Fig. 4.9 a) without post-processing. The inset shows that the intensity of $(\frac{1}{2} \frac{1}{2})$ -streaks and integer multiples hereof is negligible in comparison with, e.g., the $(0 \frac{1}{2})$ -streak.

Comparing both images, one can see that the software used to enhance the dynamic range amplifies even the weakest features. However, there are three possible reasons for the appearance of $(\frac{1}{2} \frac{1}{2})$ -streaks in Fig. 4.9 a): At first, they might originate from the line-like structure of the reconstructed Si(100) surface [102]. Second, they might result from superposition of other diffraction streaks or even KIKUCHI-lines. And third, there might be very small regions at the surface with a (2×2) -reconstruction. For instance, this may come out for the correlated buckling of Si dimers at low temperatures [14, 101], crystalline silicon carbide (SiC) [103, 104], or tin-induced reconstructions [105]. But the RHEED images were taken at RT and no other structures than the $(2 \times 1)/(1 \times 2)$ -reconstruction of the Si(100) surface could be confirmed using STM.

The reason of their existence could not be clarified unambiguously in this experiment, since no spectroscopic methods were available to check the surface for impurities. In conclusion, the $(\frac{1}{2} \frac{1}{2})$ -streaks should be treated as what they are, namely artifacts from the post-processing software. With regard to Fig. 4.10, their intensity is negligible in comparison with, e.g., the $(0 \frac{1}{2})$ -streak.

If the pattern in Fig. 4.9 b) is compared with the clean surface in Fig. 4.9 a), six additional LAUE-circles occurred. These are indicated by red, dashed circle sections and can be attributed to a crystal structure with a seven times larger surface unit cell along the $\langle \bar{1}10 \rangle / \langle 1\bar{1}0 \rangle$ crystal direction in real space. As it was already mentioned in Sec. 3.2, this is associated with the (2×7) -reconstruction of the wetting layer after deposition of REE on Si(100) surfaces [1, 85–87]. Additional spots also occurred on the perimeter of the original LAUE-circles. For a closer consideration the black frame from Fig. 4.9 b) is shown in a higher resolution in Fig. 4.11.

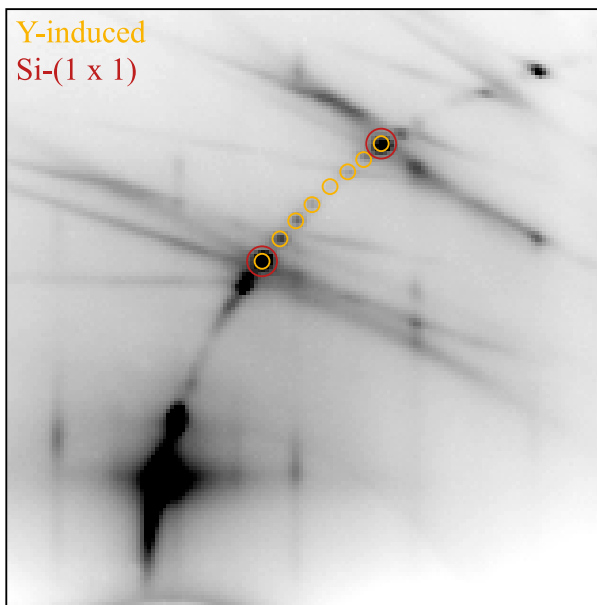


Figure 4.11: Magnification of black frame in Fig. 4.9 b). The six additional streaks (indicated by small, yellow circles) between those of the Si-(1 \times 1) (indicated by big, red circles) are associated with the $(\times 7)$ -component of the Y-induced (2×7) -reconstruction, which is caused by the growth of a wetting layer.

In this image six additional streaks (indicated in yellow) occur on the original ($L = \frac{1}{2}$) $\frac{1}{2}$ -circle between streaks of the cubic Si-(1 \times 1) (indicated in red). These can also be attributed to the $(\times 7)$ -component of the Y-induced (2×7) -reconstruction, since the nominally flat Si(100) surface exhibits terraces that are separated by single-layer step heights. Therefore, the orientation of both the dimer rows and the wetting layer after Y-deposition are rotated by 90° on neighboring terraces (cf. Fig. 3.3).

When the azimuth angle is rotated from $\gamma \approx 220^\circ$ (equivalent to the electron beam in $\langle \bar{1}10 \rangle / \langle 1\bar{1}0 \rangle$ direction) towards $\gamma \approx 255^\circ$, another RHEED pattern can be observed. This diffraction condition is displayed in Fig. 4.12 a) for the clean and in Fig. 4.12 b) for the Y-covered surface. Here, one observes several curved streaks, which are related to the strictly one-dimensional periodicity of YSi₂-nanowires [5, 106]. Furthermore, they indicate the crystallinity and good lattice match with the underlying Si substrate, since the streaks pass through the cubic (1 \times 1)-lattice of the Si(100) surface. Hence, they can also be understood as evidence for the proposed hexagonal AlB₂-structure of the wires (cf. Sec. 3.2).

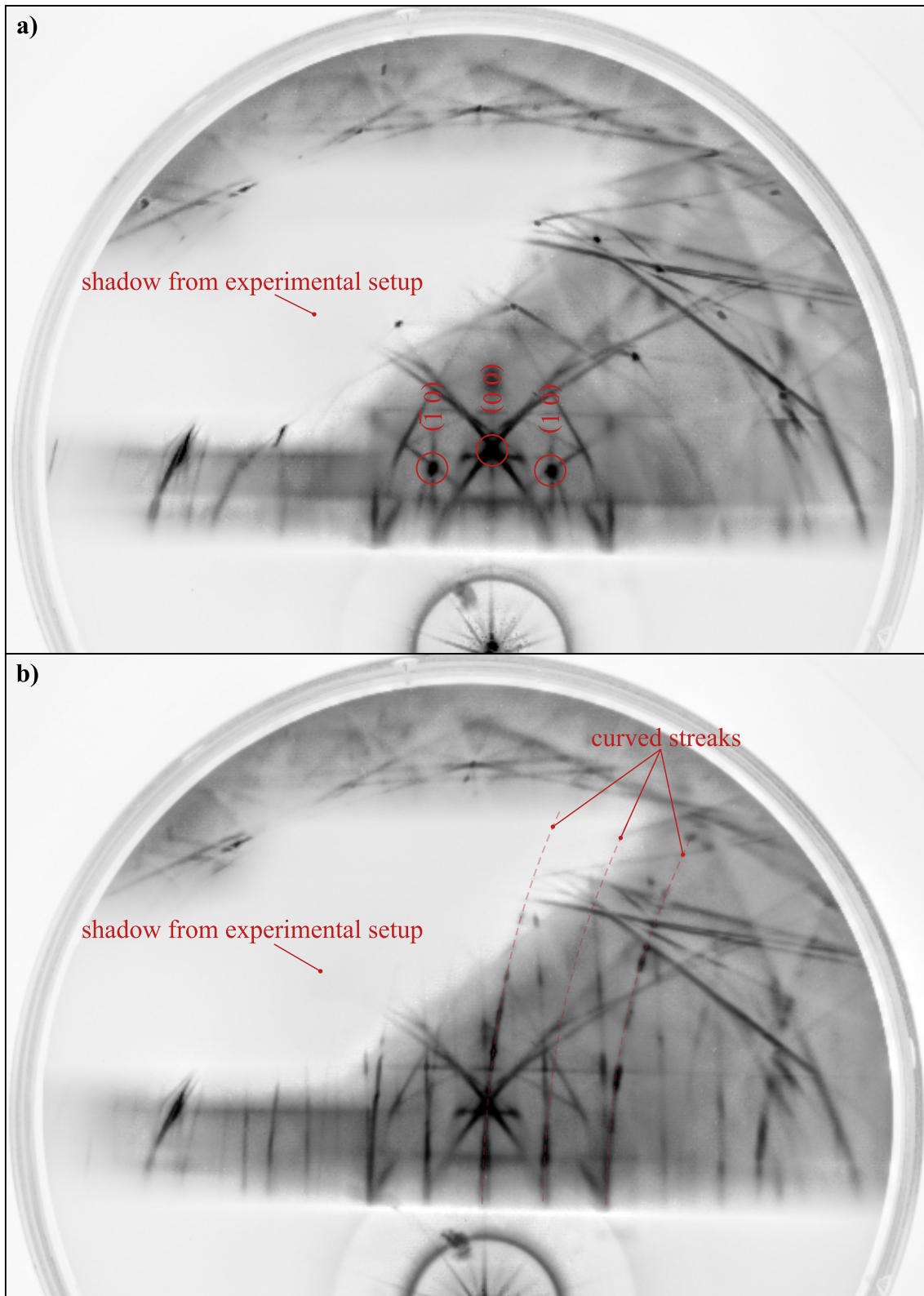


Figure 4.12: RHEED pattern with same properties as Fig. 4.9, except for the azimuth angle. Curved, parallel streaks can be understood as evidence for crystallinity of the YSi₂-nanowires and good lattice match with the Si(100) substrate [5, 106].

4.3 YSi₂ on vicinal Si(100)

4.3.1 DC heating step-parallel

In addition to nominally flat surfaces, Y was also deposited on vicinal Si(100) samples in order to grow YSi₂-nanowires. So far, it remained unclear, whether the wetting layer on this kind of surface would exhibit the same (2 × 7)-reconstruction it reveals when grown on flat samples. The reason for this is that the terraces with an average width of 3.89 nm (cf. Sec. 3.1) normally would limit the propagation of a surface-wide network. Furthermore, it is expected that any type of inter-terrace communication between Y-atoms is energetically prohibited, which would result in random starting positions of wetting layer and nanowires along the terraces. Anyway, the last sample in Sec. 4.1 with an applied DC in step-parallel direction was used for the growth of YSi₂-nanowires. The evaporating conditions were $T_{\text{dep}} \approx 625^\circ\text{C}$, the evaporating time $t_{\text{evap}} = 60\text{ s}$, and the evaporating power $P_{\text{evap}} \approx 39.9\text{ W}$. As for the nominally flat sample in Sec. 4.2, the nanowires were not exposed to any PA but quenched to RT right after the deposition. Fig. 4.13 shows diffraction patterns of the clean and silicide-covered surface, which was heated with step-parallel DC.

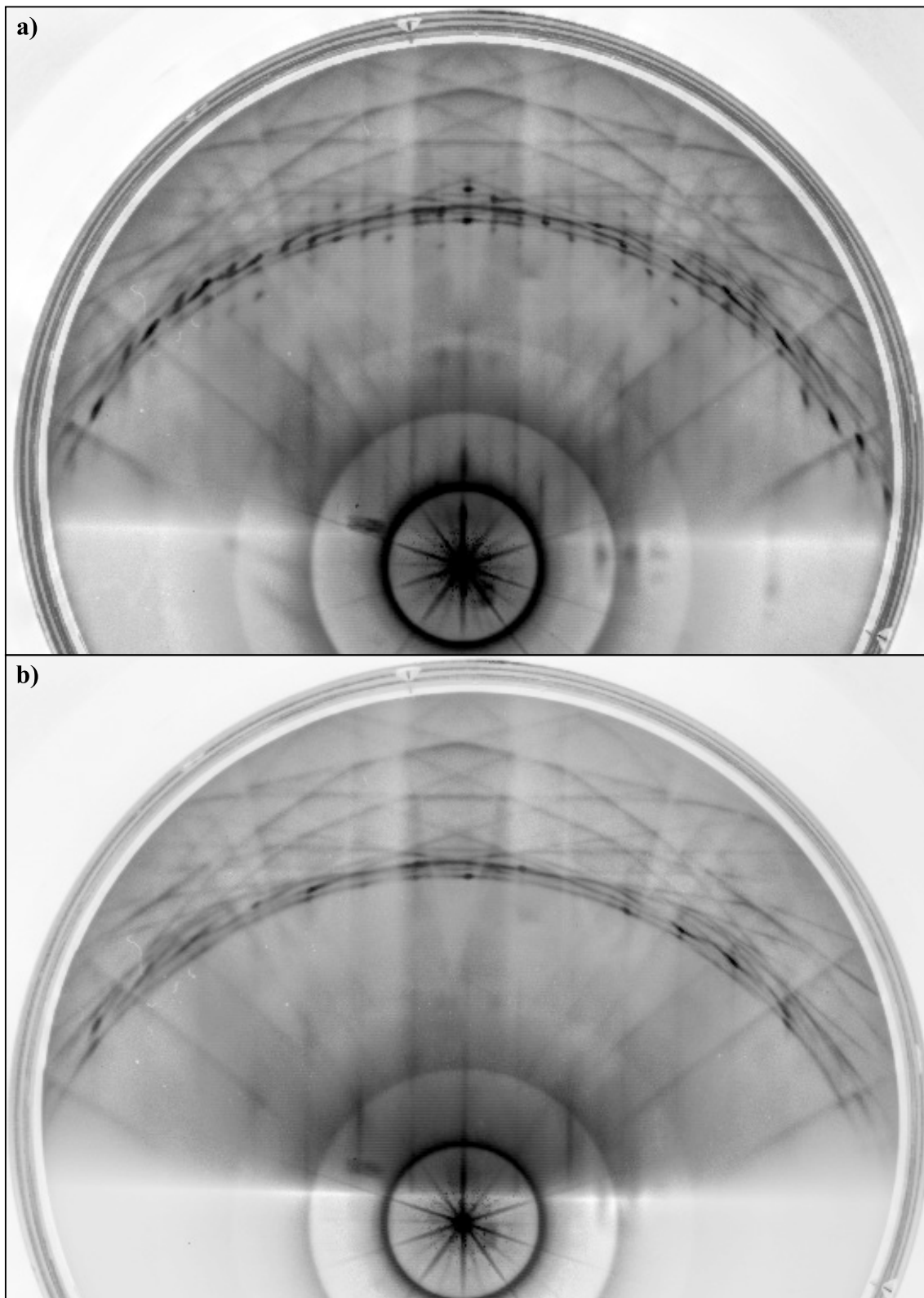


Figure 4.13: RHEED pattern (15 keV, electron beam perpendicular to the step edges, DC in step-parallel direction) of vicinal Si(100) **a)** as clean surface and **b)** with Y-coverage ($\theta \approx 0.4$ ML).

The basic features of the clean surface in Fig. 4.13 a), e.g. the split spot left and right of where would be the (0 1/2)-streak or the split (01)-streak, were discussed in Sec. 2.2.2. The very weak first order of the ($L = 1/2$)-circle was there associated with a minor (2 × 1)-domain at the surface. The weakness of the circle, however, is surprising in consideration of the STM images that were obtained from this surface (cf. Fig. 4.7). In Sec. 4.1 it was concluded that the vicinal Si(100) sample with an applied DC in step-parallel direction reveals (2 × 1)-terraces at over 15 % of the surface. But this is not reflected by these RHEED patterns. Note that the circle is weak in Fig. 4.13, but almost non-existing in the non-processed image (cf. Fig. 2.9).

Comparing Fig. 4.13 a) with Fig. 4.13 b) it attracts attention that the splitting of the (01)-streak vanished, which was associated with the vicinality of the surface [8]. Anyhow, the ($L = 1$)-circle is still existing but shows a very blurred perimeter. The remaining diffraction streaks on the circle can not be dedicated to one of the crystalline phases with certainty. Furthermore, in Fig. 4.13 a) the (1 × 2)-reconstruction of the dimers can be observed in terms of (1/2 0)- and (1/2 0)-streaks as well as integer multiples hereof. These completely disappeared after the surface was covered with about 0.4 ML Y indicating total disorder along this direction. This might be a serious argument to prove the expectations concerning random starting points of wetting layer and nanowires on neighboring terraces.

4.3.2 DC heating step-up

Additionally, Y was deposited on vicinal Si(100) surfaces with an applied DC in step-up direction. This kind of surfaces revealed the best surface qualities according the criteria in Sec. 4.1 and the minor (2 × 1)-domains with dimer rows parallel to the step edges only covered about 7.5 % of the surface. A RHEED pattern of such a surface is shown in Fig. 4.14. Here, the vicinality of the steps can be seen as streaks in Fig. 4.14 a), which are elongated along the LAUE-circles. In reality, each *elongated streak* consists of two separate spots. This can be obtained from the non-manipulated inset in Fig. 4.14 b). The diffraction pattern after Y-deposition exhibits a superstructure along the ($L = 0$)-circle. But for lack of resolution it can not be stated with certainty, if this is the expected ($\times 7$)-component of the (2 × 7)-reconstruction. The ($\times 2$)-component, however, can be derived from the blurred ($L = 1/2$)-circle. Again, no superstructure can be resolved along the circle, which indicates the randomly distributed starting points of the wetting layer.

In Fig. 4.15 the corresponding pattern to Fig. 4.12 can be seen for a sample, which was flash-heated and post-annealed with step-up DC. Since the sample was rotated by 90° between Fig. 4.15 and Fig. 4.12, the curved and parallel streaks are not covered by the experimental setup in this case. The ($L = 1$)-circle is indicated by a red, dashed circle section in Fig. 4.15 a). The ($L = 1/2$)-circle of the clean surface can be guessed, too, but is hard to indicate by hand. It should be noted that in Fig. 4.15 a) streaks at (1/2 0)- and (1/2 0)-positions as well as integer multiples hereof can be seen. Although no quantitative conclusions can be made about the true amount, one can definitely state that (2 × 1)-reconstructed surfaces are existent on the surface. These vanished after the growth of YSi₂-nanowires, which speaks for their one-dimensionality and may

Results and discussion

be indicated as overgrowth of the (2×1) -terraces in the orthogonal direction, while Si is incorporated from the sample surface into the nanowire.

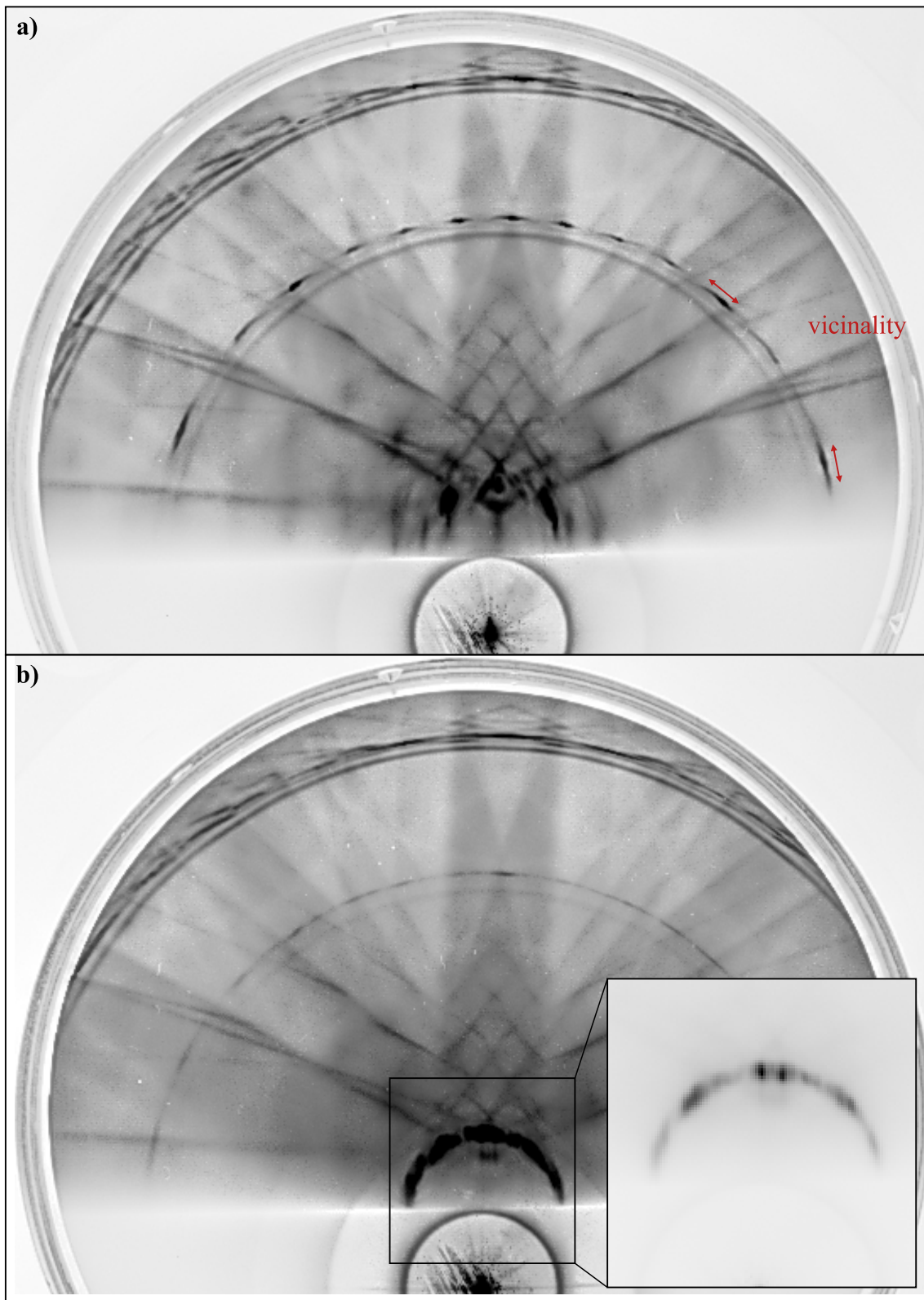


Figure 4.14: RHEED pattern (15 keV, electron beam parallel to the step edges, DC in step-up direction) of vicinal Si(100) **a)** as clean surface and **b)** with Y-coverage and non-manipulated inset of ($L = 0$)-circle ($\theta \approx 0.35$ ML).

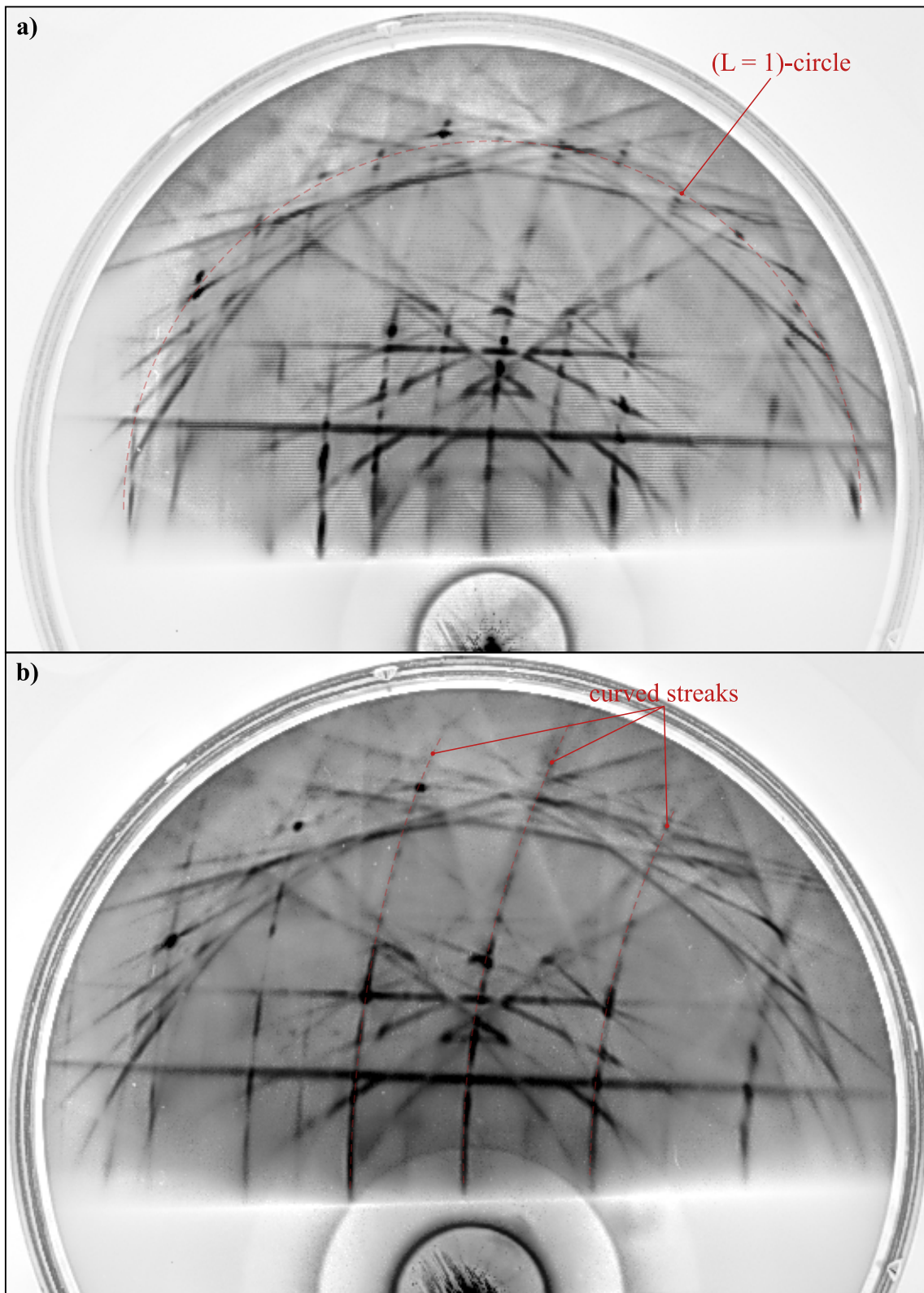


Figure 4.15: RHEED pattern with same properties as Fig. 4.14, except for the azimuth angle. Curved, parallel streaks can be understood as evidence for crystallinity of the YSi_2 -nanowires and good lattice match with the $\text{Si}(100)$ substrate [5, 106].

5 Conclusion

During this thesis the preparation of vicinal Si(100) surfaces with a miscut of 4° against $\langle 110 \rangle$ was optimized with regard to the flash-heating temperature, DC direction, and PA procedure. The goal was to find an optimum building foundation for ordered YSi₂-nanowire arrays. The different preparation procedures were controlled by STM and RHEED images.

In this context, the best possible vicinal Si(100) surface was achieved for an applied DC in step-up direction, flashing at 1250°C for multiple times, and quenching to 935°C . This was followed by 15 min of PA and a relatively slow cooling down procedure to RT with a rate of $< 1^\circ\text{C}/\text{s}$. In comparison with the other DC directions and with regard to the PA procedure, these samples offered relatively smooth surfaces with few kinks and the lowest coverage of (2×1) -domains as seen from the STM images. Furthermore, they revealed straight step edges in combination with homogenously distributed terrace widths and defect-free dimer rows over large surface areas.

From the RHEED patterns one can conclude that in consistency with the nominally flat surfaces also a (2×7) -reconstruction can be observed on the vicinal Si(100) surface, due to the wetting layer of the Y. Furthermore, the diffraction patterns exhibit similar information concerning reconstructions on the surface than the STM, but for a larger scale. However, the interpretation of dynamically extended RHEED images have to be done carefully. For instance, these revealed a (2×2) -reconstructed surface, while this could not be confirmed by corresponding STM images. In such cases, it is always helpful to consult the non-processed images (out of the box) to be able to estimate real intensity ratios of diffraction streaks.

The growth of YSi₂-nanowires was observed on two types of vicinal samples, namely with an applied DC current in step-up and in step-parallel direction. These could be compared with results from nominally flat surfaces as well. From this, a new mechanism was observed during nanowire growth on the step-parallel contacted samples. On these surfaces a single digit percentage is covered by YSi₂-nanowires perpendicular to the step edges, although the current direction and the associated electromigration would suspect a different outcome. This behavior was, however, never noticed on samples with an applied DC perpendicular to the step edges.

Some of the samples were capped with amorphous Si and investigated using Grazing Incidence X-Ray Diffraction (GIXRD). It was the aim to get detailed information about the system's structural properties, which was for the RHEED images in Chap. 4 often limited by the camera's resolution. The results, however, are still viewed but at first sight they indicate that both the atomic wires and the wetting layer were destroyed by the capping. Finding a solution for this might help to do research on the YSi₂-nanophases ex-situ.

One should also have in mind that the substrate preparation is influenced from strain applied to the surface. This is, e.g., often the case when Si samples are clamped

by the flashing contacts. It might be tough to reproduce the impact on vicinal surfaces, but strain does affect the results from flash-heating flat surfaces. With regard to the investigated material it might be interesting to investigate the growth of other RESN, e.g. dysprosium di-silicide (DySi_2). This compound is as well as the dysprosium metal known to exhibit interesting structural and magnetic behavior at low temperatures [107–111]. It might be a suitable candidate for the investigation of quasi one-dimensional magnetism in nanowires.

Bibliography

- [1] V. IANCU, P. R. C. KENT, et al.: **Structure and growth of quasi-one-dimensional YSi₂ nanophases on Si(100)**. In: *J. Phys.: Condens. Matter* **25** (2013), p. 014011. DOI: 10.1088/0953-8984/25/1/014011.
- [2] Yong CHEN, Douglas A. A. OHLBERG, and R. Stanley WILLIAMS: **Nanowires of four epitaxial hexagonal silicides grown on Si(001)**. In: *J. Appl. Phys.* **91** (2002), pp. 3213 –3218. DOI: 10.1063/1.1428807.
- [3] B. Z. LIU and J. NOGAMI: **A scanning tunneling microscopy study of dysprosium silicide nanowire growth on Si(001)**. In: *J. Appl. Phys.* **93** (2003), pp. 593 –599. DOI: 10.1063/1.1516621.
- [4] C. EAMES, M. I. J. PROBERT, and S. P. TEAR: **The structure and growth direction of rare earth silicide nanowires on Si(100)**. In: *Appl. Phys. Lett.* **96**, 241903 (2010). DOI: 10.1063/1.3453865.
- [5] S. HUS and H. H. WEITERING: **Formation of uni-directional ultrathin metallic YSi₂ nanowires on Si(110)**. In: *Appl. Phys. Lett.* **103** (2013), pp. 073101–1 –073101–3. DOI: 10.1063/1.4817529.
- [6] C. PREINESBERGER, S. K. BECKER, et al.: **Structure of DySi₂ nanowires on Si(001)**. In: *J. Appl. Phys.* **91** (2002), pp. 1695–1697. DOI: 10.1063/1.1430540.
- [7] C. PREINESBERGER, S. VANDRE, et al.: **Formation of dysprosium silicide wires on Si(001)**. In: *J. Phys. D: Appl. Phys.* **31** (1998), p. L43. DOI: 10.1088/0022-3727/31/12/001.
- [8] A. ICHIMIYA and P. I. COHEN: **Reflection High-Energy Electron Diffraction**. 1st ed. Cambridge University Press, 2004.
- [9] L. DE BROGLIE: **Recherche sur la théorie des quanta**. *PhD thesis*. Migration-université en cours d'affectation, 1924.
- [10] W. BRAUN: **Applied RHEED - Reflection High-Energy Electron Diffraction during Crystal Growth**. Springer-Verlag, 1999.
- [11] E. HECHT: **Optics**. 4th ed. Addison-Wesley, 2001.
- [12] W. DEMTRÖDER: **Lehrbuch der Experimentalphysik (Elektrizität und Optik)**. 6th ed. volume 2. Springer-Verlag, 2013.
- [13] N. PATHÉ: **Measurement techniques for diffraction and reflection of x-rays from synchrotron radiation**. In: *Seminar Talk at UOS* (2013).
- [14] K. OURA, V. G. LIFSHITS, et al.: **Surface Science: Introduction**. Springer-Verlag, 2003.

- [15] C. KITTEL: **Introduction to Solid State Physics**. 1st ed. John Wiley & Sons Inc., 1957. DOI: 10.1063/1.3060399.
- [16] K. KOPITZKI: **Einführung in die Festkörperphysik**. 1st ed. B. G. Teubner GmbH, 1986. DOI: 10.1007/978-3-8351-9127-3.
- [17] G. A. SOMORJAI and Y. LI: **Introduction to Surface Chemistry and Catalysis**. 1st ed. John Wiley & Sons Inc., 1994. DOI: 10.1002/cvde.19950010308.
- [18] W. H. BRAGG and W. L. BRAGG: **The reflection of X-rays by crystals**. In: *Proc. R. Soc. Lond. A* 88 (1913), pp. 428–438.
- [19] W. FRIEDRICH, P. KNIPPING, and M. LAUE: **Interferenzerscheinungen bei Röntgenstrahlen**. In: *Ann. d. Phys.* 346 (1913), pp. 971–988. DOI: 10.1002/andp.19133461004.
- [20] W. H. MILLER: **A treatise on crystallography**. In: *Printed at the Pitt Press for J. & JJ Deighton* (1839).
- [21] H. WILKENS: **Phase transition of rare earth oxide films grown on Si(111)**. *PhD thesis*. Universität Osnabrück, 2014.
- [22] P. P. EWALD: **Zur Theorie der Interferenzen der Röntgentstrahlen in Kristallen**. In: *Physik. Z.* 14 (1913), pp. 465–472.
- [23] J. WOLLSCHLÄGER, J. FALTA, and M. HENZLER: **Electron diffraction at stepped homogeneous and inhomogeneous surfaces**. In: *Appl. Phys. A* 50 (1990), pp. 57–68. DOI: 10.1007/BF00323955.
- [24] P. J. DOBSON, B. A. JOYCE, et al.: **Current understanding and applications of the RHEED intensity oscillation technique**. In: *J. Cryst. Growth* 81 (1987), pp. 1–8. DOI: 10.1016/0022-0248(87)90355-1.
- [25] H. BETHE: **Theorie der Beugung von Elektronen an Kristallen**. In: *Ann. d. Phys.* 392 (1928), pp. 55–129.
- [26] M. HENZLER: **The Study of Epitaxy with Spot Profile Analysis of LEED**. In: *The Structure of Surfaces II*. Springer-Verlag, 1988, pp. 431–437. DOI: 10.1007/978-3-642-73343-7_71.
- [27] M. A. van HOVE, W. H. WEINBERG, and C.-M. CHAN: **Low-Energy Electron Diffraction**. 1st ed. Springer-Verlag, 1986.
- [28] J. M. COWLEY: **Diffraction Physics**. North-Holland Publishing Company, 1975. DOI: 10.1107/S0567739476001514.
- [29] I. K. ROBINSON and D. J. TWEET: **Surface X-ray diffraction**. In: *Rep. Prog. Phys.* 55 (1992), p. 599. URL: <http://stacks.iop.org/0034-4885/55/i=5/a=002>.
- [30] M. HENZLER: **Electron Diffraction and Surface Defect Structure**. In: *Electron Spectroscopy for Surface Analysis IV*. Ed. by H. IBACH. Springer-Verlag, 1977, pp. 117–149. DOI: 10.1007/978-3-642-81099-2_4.
- [31] P. DEBYE: **Interferenz von Röntgenstrahlen und Wärmebewegung**. In: *Ann. d. Phys.* 348 (1913), pp. 49–92. DOI: 10.1002/andp.19133480105.

- [32] I. WALLER: **Zur Frage der Einwirkung der Wärmebewegung auf die Interferenz von Röntgenstrahlen.** German. In: *Z. Phys.* **17**.1 (1923), pp. 398–408. DOI: 10.1007/BF01328696.
- [33] H. METZGER, H. BEHR, and J. PEISL: **The static DEBYE-WALLER factor of defect-induced lattice displacements.** English. In: *Z. Phys. B Con. Mat.* **46** (1982), pp. 295 –299. DOI: 10.1007/BF01307703.
- [34] J. E. HOUSTON and R. L. PARK: **LEED from statistical step models.** In: *Surf. Sci.* **26** (1971), pp. 269–285. DOI: 10.1016/0039-6028(71)90126-9.
- [35] M. HENZLER: **Quantitative evaluation of random distributed steps at interfaces and surfaces.** In: *Surf. Sci.* **73** (1978), pp. 240–251. DOI: 10.1016/0039-6028(78)90499-5.
- [36] J. E. HOUSTON and R. L. PARK: **Low-energy electron diffraction from imperfect structures.** In: *Surf. Sci.* **21** (1970), pp. 209–223. DOI: 10.1016/0039-6028(70)90228-1.
- [37] F. BERTRAM: **The structure of ultrathin iron oxide films studied by x-ray diffraction.** *PhD thesis.* Universität Osnabrück, 2012.
- [38] S. NISHIKAWA and S. KIKUCHI: **Diffraction of cathode rays by mica.** In: *Proc. Im. Acad. Jpn* **4** (1928), pp. 271–274. DOI: 10.1038/1211019a0.
- [39] C. J. DAVISSON and L. H. GERMER: **The Scattering of Electrons by a Single Crystal of Nickel.** In: *Nature* **119** (1927), pp. 558–560.
- [40] C. J. DAVISSON and L. H. GERMER: **Diffraction of Electrons by a Crystal of Nickel.** In: *Phys. Rev.* **30** (1927), pp. 705–740. DOI: 10.1103/PhysRev.30.705.
- [41] G. P. THOMSON: **Experiments on the Diffraction of Cathode Rays.** In: *Proc. R. Soc. London* **117** (1928), pp. 600–609. URL: <http://www.jstor.org/stable/94980>.
- [42] G. P. THOMSON: **The early history of electron diffraction.** In: *Contemporary Physics* **9** (1968), pp. 1–15.
- [43] A. Y. CHO: **Morphology of Epitaxial Growth of GaAs by a Molecular Beam Method: The Observation of Surface Structures.** In: *J. Appl. Phys.* **41** (1970), pp. 2780–2786. DOI: 10.1063/1.1659315.
- [44] J. H. NEAVE, B. A. JOYCE, et al.: **Dynamics of film growth of GaAs by MBE from Rheed observations.** English. In: *Appl. Phys. A* **31** (1983), pp. 1 –8. DOI: 10.1007/BF00617180.
- [45] G. ERES: **Fundamental Limits of Interface Sharpness in Complex Oxide Film Growth.** In: *Seminar Talk at UTK* (2013). URL: <http://wcms-neu1.urz.uni-halle.de/download.php?down=29697&elem=2680049>.
- [46] S. Y. HU, J. C. YI, et al.: **Serpentine Superlattice Nanowire-Array Lasers.** In: *IEEE J. Quant. Elect.* **31** (1995), pp. 1380 –1388.

- [47] P. R. PUKITE, C. S. LENT, and P. I. COHEN: **Diffraction from stepped surfaces: II. Arbitrary terrace distributions.** In: *Surf. Sci.* **161** (1985), pp. 39–68. DOI: 10.1016/0039-6028(85)90727-7.
- [48] C. J. CHEN: **Introduction to Scanning Tunneling Microscopy.** Oxford University Press, 2008.
- [49] H. EISELE: **Cross-Sectional Scanning Tunneling Microscopy of InAs/GaAs Quantum Dots.** *PhD thesis.* Technische Universität Berlin, 2001.
- [50] R. H. FOWLER and L. NORDHEIM: **Electron Emission in Intense Electric Fields.** In: *Proc. R. Soc. London* **119** (1928), pp. 173–181.
- [51] G. BINNIG, H. ROHRER, et al.: **Tunneling through a controllable vacuum gap.** In: *Appl. Phys. Lett.* **40** (1982), pp. 178–180. DOI: 10.1063/1.92999.
- [52] G. BINNIG and H. ROHRER: **Scanning Tunneling Microscopy.** In: *Helv. Phys. Acta* **55** (1982), pp. 726–735.
- [53] R. TIMM: **Rastertunnelmikroskopie an Querschnittsflächen von Typ-II Quantentöpfen.** *PhD thesis.* Technische Universität Berlin, 2002.
- [54] S. JENTSCH: **Anfangsstadien des epitaktischen Wachstums von Eisen-oxidfilmen auf Ag(001).** *Master's thesis.* Universität Osnabrück, 2012.
- [55] L. D. LANDAU and E. M. LIFSHITZ: **Course of Theoretical Physics 3 (Quantum Mechanics).** Pergamon Press, 1992.
- [56] W. NOLTING: **Grundkurs Theoretische Physik 5 (Quantenmechanik).** Springer-Verlag, 2008.
- [57] J. BARDEEN: **Tunnelling from a Many-Particle Point of View.** In: *Phys. Rev. Lett.* **6** (2 1961), pp. 57 –59. DOI: 10.1103/PhysRevLett.6.57.
- [58] J. TERSOFF and D. R. HAMANN: **Theory and application for the scanning tunneling microscope.** In: *Phys. Rev. Lett.* **50** (1983), pp. 1998 –2001.
- [59] C. J. CHEN: **Microscopic view of scanning tunneling microscopy.** In: *J. Vac. Sci. Technol. A* **9** (1991), pp. 44 –50. DOI: 10.1116/1.577128.
- [60] C. J. CHEN and R. J. HAMERS: **Role of atomic force in tunneling-barrier measurements.** In: *J. Vac. Sci. Technol. B* **9** (1991), pp. 503 –505. DOI: 10.1116/1.585556.
- [61] G. BINNIG and H. ROHRER: **Scanning Tunneling Microscopy.** In: *IBM Journal of Research and Development* **30** (1986), pp. 3–4.
- [62] E. RUSKA, G. BINNIG, and H. ROHRER: **Press Release for The Nobel Prize in Physics 1986.** The Royal Swedish Academy of Sciences. October 15th, 1986. URL: http://www.nobelprize.org/nobel_prizes/physics/laureates/1986/press.html.
- [63] R. WIESENDANGER: **Scanning Probe Microscopy and Spectroscopy.** Cambridge University Press, 1994.
- [64] F. MOHN, L. GROSS, et al.: **Imaging the charge distribution within a single molecule.** In: *Nature Nanotechnology* **7** (2012), pp. 227–231. DOI: 10.1038/nnano.2012.20.

- [65] A. N. CHAIKA, S. S. NAZIN, et al.: **High resolution STM imaging with oriented single crystalline tips**. In: *Appl. Surf. Sci.* **267** (2013). 11th International Conference on Atomically Controlled Surfaces, Interfaces and Nanostructures, pp. 219 –223. DOI: 10.1016/j.apsusc.2012.10.171.
- [66] G. BINNIG and D. P. E. SMITH: **Singletube threedimensional scanner for scanning tunneling microscopy**. In: *Rev. Sci. Instrum.* **57** (1986), pp. 1688–1689. DOI: 10.1063/1.1139196.
- [67] L. JURCZYSZYN, N. MINGO, and F. FLORES: **The influence of the geometry of the tip on the STM images**. English. In: *Czech. J. Phys.* **47** (1997), pp. 407–413. DOI: 10.1023/A:1021255005699.
- [68] L. JURCZYSZYN, N. MINGO, and F. FLORES: **Influence of the atomic and electronic structure of the tip on STM images and STS spectra**. In: *Surf. Sci.* **402 - 404** (1998), pp. 459 –463. DOI: 10.1016/S0039-6028(97)00971-0.
- [69] R. ZHANG and D. G. IVEY: **Preparation of sharp polycrystalline tungsten tips for scanning tunneling microscopy imaging**. In: *J. Vac. Sci. Technol. B* **14** (1996), pp. 1 –10. DOI: 10.1116/1.589029.
- [70] T. SAKURAI, T. HASHIZUME, et al.: **Field ion-scanning tunneling microscopy**. In: *Prog. Surf. Sci.* **33** (1990), pp. 3 –89. DOI: 10.1016/0079-6816(90)90012-9.
- [71] C. CHIUTU, A. M. SWEETMAN, et al.: **Precise Orientation of a Single C₆₀ Molecule on the Tip of a Scanning Probe Microscope**. In: *Phys. Rev. Lett.* **108** (2012), pp. 268302 –268307. DOI: 10.1103/PhysRevLett.108.268302.
- [72] A. SWEETMAN, S. JARVIS, et al.: **Effect of the tip state during qPlus noncontact atomic force microscopy of Si(100) at 5 K: Probing the probe**. In: *Beilst. J. Nanotech.* **3** (2012), pp. 25 –32. DOI: 10.3762/bjnano.3.3.
- [73] S. GEVERS: **Praseodymia on non-passivated and passivated Si(111) surfaces**. *PhD thesis*. Universität Osnabrück, 2010.
- [74] R. NAVÉ: **Abundances of the Elements in the Earth's Crust**. Georgia State University. March 23rd, 2014. URL: <http://hyperphysics.phy-astr.gsu.edu/hbase/tables/elabund.html>.
- [75] R. E. SCHLIER and H. E. FARNSWORTH: **Structure and Adsorption Characteristics of Clean Surfaces of Germanium and Silicon**. In: *J. Chem. Phys.* **30** (1959), pp. 917 –920.
- [76] D. J. CHADI: **Stabilities of single-layer and bilayer steps on Si(001) surfaces**. In: *Phys. Rev. Lett.* **59** (15 1987), pp. 1691 –1694. DOI: 10.1103/PhysRevLett.59.1691.
- [77] O. L. ALERHAND, A. N. BERKER, et al.: **Finite-temperature phase diagram of vicinal Si(100) surfaces**. In: *Phys. Rev. Lett.* **64** (20 1990), pp. 2406 –2409. DOI: 10.1103/PhysRevLett.64.2406.

- [78] B. S. SWARTZENTRUBER, Y. W. MO, et al.: **Scanning tunneling microscopy studies of structural disorder and steps on Si surfaces**. In: *J. Vac. Sci. Technol. A* 7 (1989), pp. 2901 –2905. DOI: 10.1116/1.576167.
- [79] S. STOYANOV: **Heating Current Induced Conversion between 2×1 and 1×2 Domains at Vicinal (001) Si Surfaces - Can it be Explained by Electromigration of Si Adatoms?** In: *Jpn. J. Appl. Phys.* 29 (1990), pp. 659 –662. DOI: 10.7567/JJAP.29.L659.
- [80] L. V. LITVIN, A. B. KRASILNIKOV, and A. V. LATYSHEV: **Transformations of the stepped Si(001) surface structure induced by heating the specimen by a current**. In: *Surf. Sci. Lett.* 244 (1991), pp. 121 –124. DOI: 10.1016/0167-2584(91)90713-2.
- [81] S. STOYANOV: **Electromigration Induced Step Bunching on Si Surfaces - How Does it Depend on the Temperature and Heating Current Direction?** In: *Jpn. J. Appl. Phys.* 30 (1991), pp. 1 –6. DOI: 10.7567/JJAP.30.1.
- [82] M. ICHIKAWA and T. DOI: **Study of Si(001) 2×1 domain conversion during direct current and radiative heatings**. In: *Appl. Phys. Lett.* 60 (1992), pp. 1082 –1084. DOI: 10.1063/1.106451.
- [83] B. S. SWARTZENTRUBER, N. KITAMURA, et al.: **Behavior of steps on Si (001) as a function of vicinality**. In: *Phys. Rev. B* 47 (1993), pp. 13432 –13441. DOI: 10.1103/PhysRevB.47.13432.
- [84] F. H. SPEDDING, A. H. DAANE, and K. W. HERRMANN: **The crystal structures and lattice parameters of high-purity scandium, yttrium and the rare earth metals**. In: *Acta Crystallogr.* 9 (1956), pp. 559 –563. DOI: 10.1107/S0365110X5600156X.
- [85] B. Z. LIU and J. NOGAMI: **An STM study of the Si(001) (2 x 7)-Gd, Dy surface**. In: *Surf. Sci.* 540 (2003), pp. 136 –144. DOI: 10.1016/S0039-6028(03)00826-4.
- [86] C. ZENG, P. R. C. KENT, et al.: **Charge-order fluctuations in one-dimensional silicides**. In: *Nature Materials* 7 (2008), pp. 539 –542. DOI: 10.1038/nmat2209.
- [87] V. IANCU, P. R. C. KENT, et al.: **Structure of YSi₂ nanowires from scanning tunneling spectroscopy and first principles**. In: *Appl. Phys. Lett.* 95, 123107 (2009). DOI: 10.1063/1.3236778.
- [88] K. OURAY and T. HANAWA: **LEED-AES study of the Au-Si(100) system**. In: *Surf. Sci.* 82 (1979), pp. 202 –214. DOI: 10.1016/0039-6028(79)90328-5.
- [89] T. ICHIKAWA and S. INO: **Double diffraction spots in RHEED patterns from clean Ge(111) and Si(001) surfaces**. In: *Surf. Sci.* 85 (1979), pp. 221 –243. DOI: 10.1016/0039-6028(79)90247-4.
- [90] S. OKADA, K. OURAY, et al.: **A leed-aes study of thin Pd films on Si(111) and (100) substrates**. In: *Surf. Sci.* 97 (1980), pp. 88 –100. DOI: 10.1016/0039-6028(80)90105-3.

- [91] A. KAWAZU, T. OTSUKI, and G. TOMINAGA: **Growth of Bismuth Layers on Si(100) Surfaces**. In: *Jpn. J. Appl. Phys.* **20**.3 (1981), pp. 553 –560. DOI: 10.7567/JJAP.20.553. URL: <http://jjap.jsap.jp/link?JJAP/20/553/>.
- [92] M. HANBÜCKEN and H. NEDDERMEYER: **A LEED - AES study of the growth of Ag films on Si(100)**. In: *Surf. Sci.* **114** (1982), pp. 563 –573. DOI: 10.1016/0039-6028(82)90705-1.
- [93] M. HANBÜCKEN, H. NEDDERMEYER, and J. A. VENABLES: **Surface cleaning of Si(100) and Ag/Si(100): Characterisation by SEM, AES and RHEED**. In: *Surf. Sci. Lett.* **137** (1984), pp. L92 –L96. DOI: 10.1016/0167-2584(84)90871-5.
- [94] A. KIRAKOSIAN, R. BENNEWITZ, et al.: **Atomically accurate Si grating with 5.73 nm period**. In: *Appl. Phys. Lett.* **79** (2001), pp. 1608 –1610. DOI: 10.1063/1.1401788.
- [95] M. ICHIKAWA and T. DOI: **Observation of electromigration effect upon Si-MBE growth on Si(001) surface**. In: *Vacuum* **41** (1990), pp. 933 –937. DOI: 10.1016/0042-207X(90)93826-5.
- [96] S. STOYANOV, H. NAKAHARA, and M. ICHIKAWA: **Dynamics of Step Bunching Induced by DC Resistive Heating of Si Wafer**. In: *Jpn. J. Appl. Phys.* **33** (1994), pp. 254 –259. DOI: 10.7567/JJAP.33.254.
- [97] A. V. LATYSHEV, L. V. LITVIN, and A. L. ASEEV: **Peculiarities of step bunching on Si(001) surface induced by DC heating**. In: *Appl. Surf. Sci.* **130 - 132** (1998), pp. 139 –145. DOI: 10.1016/S0169-4332(98)00040-3.
- [98] K. FUJITA, M. ICHIKAWA, and S. STOYANOV: **Size-scaling exponents of current-induced step bunching on silicon surfaces**. In: *Phys. Rev. B* **60** (23 1999), pp. 16006 –16012. DOI: 10.1103/PhysRevB.60.16006.
- [99] N. ROBERTS and R. J. NEEDS: **Total energy calculations of dimer reconstructions on the silicon (001) surface**. In: *Surf. Sci.* **236** (1990), pp. 112 –121. DOI: 10.1016/0039-6028(90)90765-Z.
- [100] G. BROCKS, P. KELLY, and R. CAR: **Binding and diffusion of a Si adatom on the Si(100) surface**. In: *Phys. Rev. Lett.* **66** (13 1991), pp. 1729 –1732. DOI: 10.1103/PhysRevLett.66.1729.
- [101] A. RAMSTAD, G. BROCKS, and P. KELLY: **Theoretical study of the Si(100) surface reconstruction**. In: *Phys. Rev. B* **51** (20 1995), pp. 14504 –14523. DOI: 10.1103/PhysRevB.51.14504.
- [102] S. HUS: **Personal Communication**. 2014.
- [103] T. YOSHINOBU, I. IZUMIKAWA, et al.: **Dynamic RHEED observation of 3C-SiC(001) surface reconstruction under Si₂H₆ beam irradiation**. In: *Appl. Phys. Lett.* **59** (1991), pp. 2844 –2846. DOI: 10.1063/1.105852.
- [104] J. M. POWERS, A. WANDER, et al.: **Structural analysis of the β -SiC(100)-c(2 × 2) surface reconstruction by automated tensor low-energy electron diffraction**. In: *Phys. Rev. B* **44** (20 1991), pp. 11159 –11166. DOI: 10.1103/PhysRevB.44.11159.

- [105] A. A. BASKI, C. F. QUATE, and J. NOGAMI: **Tin-induced reconstructions of the Si(100) surface**. In: *Phys. Rev. B* **44** (20 1991), pp. 11167 –11177. DOI: [10.1103/PhysRevB.44.11167](https://doi.org/10.1103/PhysRevB.44.11167).
- [106] P. DELESCLUSE and A. MASSON: **Diffuse scattering in RHEED induced by linear disorders of sulphur segregated on nickel (111) surface**. In: *Surf. Sci.* **100** (1980), pp. 423 –438. DOI: [10.1016/0039-6028\(80\)90383-0](https://doi.org/10.1016/0039-6028(80)90383-0).
- [107] J. R. BANISTER, S. LEGVOLD, and F. H. SPEDDING: **Structure of Gd, Dy, and Er at low temperatures**. In: *Phys. Rev.* **94** (1954), pp. 1140 –1142.
- [108] S. LEGVOLD, F. H. SPEDDING, et al.: **Some magnetic and electrical properties of Gd, Dy, and Er metals**. In: *Rev. Mod. Phys.* **25** (1954), pp. 129 –130.
- [109] J. PIERRE, B. LAMBERT-ANDRON, and J. L. SOUBEYROUX: **Magnetic structures of rare earth silicides RSi_{2-x} (R = Nd, Ho, Dy)**. In: *Journal of Magnetism and Magnetic Materials* **81** (1989), pp. 39 –46. DOI: [10.1016/0304-8853\(89\)90226-6](https://doi.org/10.1016/0304-8853(89)90226-6).
- [110] S. LABROO and N. ALI: **Magnetism of rare-earth disilicides**. In: *J. Appl. Phys.* **67** (1990), pp. 4811 –4813. DOI: [10.1063/1.344770](https://doi.org/10.1063/1.344770).
- [111] A. TRAVLOS, N. SALAMOURAS, and N. BOUKOS: **Epitaxial dysprosium silicide films on silicon: growth, structure and electrical properties**. In: *Thin Solid Films* **397** (2001), pp. 138 –142. DOI: [10.1016/S0040-6090\(01\)01417-1](https://doi.org/10.1016/S0040-6090(01)01417-1).